ELSEVIER

Contents lists available at ScienceDirect

# Journal of Manufacturing Processes

journal homepage: www.elsevier.com/locate/manpro





# Grinding performance and parameter optimization of laser DED TiC reinforced Ni-based composite coatings

Liaoyuan Chen<sup>a</sup>, Juncai Li<sup>b</sup>, Zhelun Ma<sup>b</sup>, Chuang Jiang<sup>a</sup>, Tianbiao Yu<sup>b,\*</sup>, Ruijie Gu<sup>a,\*</sup>

- <sup>a</sup> School of Mechatronics Engineering, Henan University of Science and Technology, Luoyang, China
- <sup>b</sup> School of Mechanical Engineering and Automation, Northeastern University, Shenyang, China

# ARTICLE INFO

Keywords:
Grinding performance
Parameter optimization
Laser DED
TiC ceramic
Surface roughness
Grinding force

#### ABSTRACT

Laser directed energy deposition (DED) in situ synthesized ceramic-reinforced composite coatings exhibit great potential for application in the surface strengthening or remanufacturing of critical components. However, the step and sticky powder effects of composite coatings result in poor surface quality. Therefore, it is of great significance to study the grinding machinability of composite coatings and to improve their surface quality. In this study, laser DED TiC reinforced Ni-based composite coatings were synthesized in situ by adding Ti and Nicoated graphite powder to the Ni-based alloy. Besides their microstructures and properties were analyzed to provide support for grinding machinability analysis. Subsequently, the effects of the grinding speed, feed rate, and cutting depth on the surface quality and grinding force were investigated using variance and signal-to-noise ratio analysis. Finally, Taguchi and grey correlation analyses were applied for the multi-objective optimization of the grinding parameters. The surface roughness (Ra), and tangential and normal grinding forces using the optimized process parameters are decreased by at least 7.18 %, 4.28 %, and 2.35 %, respectively. The ground surface was dominated by continuous plow-like grooves, and no craters or bumps caused by brittle spalling were observed. The bonding strength between the ceramic particles and matrix in the in situ synthesized composite coating was significantly improved. The peeling and extraction of ceramic particles on the ground surface were significantly decreased, resulting in surface roughness as low as 0.543 µm. In summary, laser DED in situ ceramic-reinforced composite coatings exhibit good machinability, providing theoretical and technical support for further practical applications.

# 1. Introduction

Because of the combined benefits of the toughness of the metal matrix, the wear resistance of ceramic particles, and the advantages of rapid prototyping, laser directed energy deposition (DED) ceramic reinforced composite coatings have been widely applied to surface strengthening or remanufacturing in aerospace, rail transportation, marine vessels, and advanced mechanical equipment [1–3]. In625 nickel-based alloys strengthened in solid solutions exhibit excellent mechanical strength and corrosion resistance at temperatures up to 650 °C [4,5]. Titanium carbide (TiC) ceramic is considered to be an ideal reinforcing phase for Ni-based composite coatings because of its natural wettability with nickel and high hardness (3200 kg·mm $^{-2}$ ), high melting point (3430 K), low coefficient of thermal expansion (7.74 ×  $10^{-6}$  K $^{-1}$ ) and sufficiently low density (4.93 g·cm $^{-3}$ ) [6–8]. However, the layer-by-

layer buildup characteristics and melt pool splashing behavior of laser DED result in significant step effects and large roughness on the surface of TiC reinforced Ni-based composite coatings [5,9].

To improve the surface quality of ceramic reinforced composite coatings, many studies have been carried out on the optimization of process parameters, application of energy field, and preheating process. Muvvala et al. [10] employed a high-speed camera to obtain the dimensions and lifetime of the melt pool of laser DED TiC ceramic reinforced composite coatings. The relationship between process parameters and mechanical properties was found. As the scanning speed increased, the melt pool lifetime decreased. The wetting between TiC and the matrix would be significantly decreased. Zhang et al. [11] fabricated TiC-TiB<sub>2</sub> reinforced composite coatings using ultrasound-assisted vibratory laser cladding. The effects of ultrasonic vibration on dilution, profile appearances, microstructure, and high-temperature

E-mail addresses: lychen8790@haust.edu.cn (L. Chen), m18524403828@163.com (J. Li), mazl@me.neu.edu.cn (Z. Ma), jiangchuang0379@163.com (C. Jiang), tianbiaoyudyx@gmail.com (T. Yu), jackgu0214@163.com (R. Gu).

https://doi.org/10.1016/j.jmapro.2024.12.043

Received 20 April 2024; Received in revised form 15 July 2024; Accepted 19 December 2024 Available online 3 January 2025

1526-6125/© 2024 The Society of Manufacturing Engineers. Published by Elsevier Ltd. All rights are reserved, including those for text and data mining, AI training, and similar technologies.

<sup>\*</sup> Corresponding authors.

oxidation resistance were analyzed. Results indicate that the surfaces of the composite coatings under ultrasonic vibrations are smoother and the amount of protrusion is significantly decreased. Zhang et al. [5] compared the effects of conventional and ultra-high-speed laser cladding on the surface quality of TiC reinforced In625 composite coatings. The results found that the line roughness (Ra) of the conventional laser cladding composite coating is 35.43 µm, while the smallest surface roughness of 11.75 µm is achieved when the deposition rate is 49.8 m/ min. Although scholars have carried out a lot of attempts to improve the surface quality of composite coatings and avoid secondary machining by optimizing process parameters and coating types, the surface roughness (Ra) of composite coatings is still as high as 10  $\mu$ m [12]. As the surface quality of laser cladding composite coatings is dominated by spot diameter and the width of a single track, the surface quality of composite coatings that are fabricated with large spot laser diameters is often poorer [13,14]. It is difficult to achieve high-precision assembly of fitted interfaces because of poor dimensional accuracy and surface roughness. Therefore, the laser DED composite coatings have to be secondary mechanically to further improve surface quality.

Qiao et al. [15] investigated the machinability of laser-additively manufactured TiC reinforced Ti matrix composites. Compared to coarse ceramic particles, the fine isometric TiC contributes to reducing tool wear and improving surface quality. Shu et al. [16] first compared the milling force, surface morphology, roughness, subsurface microstructure, and microhardness of conventional and laser additively manufactured high-temperature alloys. Because of finer grain and higher density of dislocations, the average cutting forces for laseradditively manufactured high-temperature alloys are 1.52-16.69 N higher than those of conventionally forged high-temperature alloys. Ding et al. [17,18] carried out experiments on conventional and ultrasonic grinding of particle-reinforced composites. The normal grinding force is decreased from 11.7 % to 9 % with the aid of ultrasonic vibration. To investigate the removal mechanism of Al alloy matrix and SiC particles, Gong et al. [19,20] conducted a series of simulated and experimental studies on the grinding performance of particle-reinforced composite coatings. The results show that a smaller cutting depth and larger grinding speed should be preferred to increase the surface quality of the ground composite material. Zhang et al. [21] investigated the grinding performance of selective laser melted (SLM) high entropy alloys and analyzed the effects of grinding parameters, processing methods, powder types, and element types on the surface morphologies, and subsurface microstructure. As the grinding speed increases and the grinding depth and feed decrease, the surface roughness (Ra) decreases and the surface quality is significantly improved. Zhou et al. [22] investigated the mechanical removal mechanism of SiCp/Al composites under ultrasonic vibration. The effects of tool vibration and removal speed on particle deformation were evaluated by scratch test. The results showed that ultrahigh-speed cutting (200 mm/min) technology is conducive to obtaining the excellent processing performance of SiCp/Al composites. Qiao et al. [23] investigated the high-speed grinding performance of SLM TiC reinforced titanium composites. With the help of high-speed grinding, no significant particle fragmentation or pull-out was observed on the ground surfaces. The smearing features are dominated on the ground surface at lower grinding speeds. When the grinding speed was 133.82 m/s, the surface roughness (Ra) was as low as 0.240 μm.

Above all, compared to single alloy materials, ground surface quality is more difficult to control because of the random distribution of ceramic particles inside laser DED composite coatings [15,24]. Besides, the bonding force at the melt pool boundary of laser DED composite coatings is often smaller than the cohesive force of the material, which can result in discontinuity strain even under continuous stress during the grinding process [21,25]. Therefore, this study investigates the grinding performance of laser DED TiC ceramic reinforced Ni-based composite coatings. The multi-objective optimization of the grinding process parameters was carried out. Firstly, in situ TiC ceramic reinforced nickel-

based composite coatings were fabricated by laser DED system. The microstructure and mechanical properties were analyzed. Secondly, the orthogonal table was designed for grinding experiments based on the Taguchi method. The grinding speed, feed rate, and cutting depth were chosen as the control factors, and the grinding characteristics (tangential, normal grinding force, and surface roughness) were adopted as the response objectives. Finally, the optimized grinding process parameter for three response objectives was combined based on the grey correlation theory and experimentally verified. Moreover, the grinding mechanism of laser DED TiC ceramic reinforced Ni-based composite coatings was also investigated. This study is expected to expand the application of laser DED ceramic reinforced composite coatings for surface strengthening or remanufacturing on critical parts and provide technical references for industrial applications.

# 2. Multi-objective optimization process

To analyze the effects of key process parameters (grinding speed, feed rate, and cutting depth) on the surface roughness (*Ra*) and grinding force of laser DED ceramic reinforced composite coatings, and to obtain the applicable parameters combinations based on grey correlation theory, a series of progressive work was carried out in this study. The result analysis and optimization were performed with the help of Minitab Statistical Software. The detailed process is as follows:

# (1) Define optimization objectives;

Surface roughness (*Ra*) is considered to be an important parameter in assessing machining accuracy. Besides, the ground surface burn and subsurface damage are mainly affected by the grinding force. It is generally accepted that lower cutting forces result in better-machined surface quality [26,27]. Therefore, surface roughness (*Ra*), tangential force (*Ft*), and normal grinding force (*Fn*) are selected as the response objectives in this study.

# (2) Select the parameter ranges and design the experiments;

Combining the advantages of the orthogonal principle and mathematical statistics, the orthogonal experiments are designed with the help of the Taguchi method. Besides, a series of one-factor experiments were carried out to identify the relatively reasonable levels of factors for the orthogonal experiment. The grinding speed was selected from 10 to 25 m/s in 5 m/s linear increments. The feed rate was selected from 1 to 4 m/min in linear increments of 1 m/min. The cutting depth was selected from 15 to 60  $\mu m$  in linear increments of 15  $\mu m$ . A matrix of 16 sets of orthogonal experiments containing 3 factors and 4 levels is obtained, as shown in Table 1.

# (3) Conducte analysis of variance (ANOVA) and F-test;

Analysis of variance (ANOVA) was employed to assess the effect level and contribution rate of each factor to the response objective [28]. Degrees of freedom (DF), the sum of squares ( $SS_F$ ), mean square ( $MS_F$ ), and percentage contribution of factors (C) are obtained according to Eqs. (1)–(6), respectively:

**Table 1**Factor and corresponding levers for grinding TiC reinforced Ni-based composite coatings.

Control factors	Symbols	Level				
		Levels	1	2	3	4
Griding speed (m/s)	$v_s$	4	10	15	20	25
Feed rate (m/min)	$ u_{ m w}$	4	1	2	3	4
Cutting depth (µm)	$a_{\rm p}$	4	15	30	45	60

i) DF can be expressed as:

$$DF = n - 1 \tag{1}$$

ii) The total  $SS_F$  can be expressed as:

$$SS_T = \sum_{i=1}^{Z} \eta_i^2 - \frac{1}{z} \left( \sum_{i=1}^{Z} \eta_i \right)^2$$
 (2)

where z is the total number of experimental groups,  $\eta_i$  s the characterization result of the  $i_{th}$  experiment.

iii) The  $SS_F$  for each test factor can be expressed as:

$$SS_F = \sum_{y=1}^{x} \frac{\left(S_{\eta_y}\right)^2}{x} - \frac{1}{z} \left(\sum_{i=1}^{z} \eta_i\right)^2$$
 (3)

where F denotes one of the test factors, y is the number of levels of factor, x denotes the number of repetitions of factor F, and  $S_{ny}$  denotes the total number of levels involving that factor.

iv) The mean value of  $MS_F$  can be expressed as follows:

$$MS_F = \frac{SS_F}{DF} \tag{4}$$

v) *C* denotes the contribution of the process parameters to each response objective and can be expressed as:

$$C = \frac{SS_F}{MS_F} \cdot 100\% \tag{5}$$

vi) The F-test for the parameter is denoted by:

$$F_{test} = \frac{MS_F}{MS_-} \tag{6}$$

where  $MS_E$  denotes mean square error.

The *F*-test is an important criterion to obtain the degree of effect of each factor on the deposition characteristics, and the judgment results are shown in Table 2. According to the  $L_{25}$  (3<sup>5</sup>) orthogonal table [29],  $F_{0.01}$ ,  $F_{0.05}$ , and  $F_{0.1}$  are 12.01, 5.41, and 3.62, respectively.

(4) Carry out signal-to-noise ratio (SNR) analysis;

The SNR is an important index for evaluating the robust stability of the process, which can reveal the effect level of the factor on the response objective [30]. *SNR* can be categorized into three types, the larger the better (*LTB*), the smaller the better (*STB*), and the more standard the better (*NTB*). Therefore, SNR can be calculated by using Eq. (7):

**Table 2**Judgements of process on deposition characteristics.

Rang	Criterion	Symbols
$F > F_{0.01}$	Extremely significant impact	***
$F_{0.01} > F > F_{0.05}$	Significant impact	***
$F_{0.05} > F > F_{0.1}$	General impact	**
$F < F_{0.1}$	Less impact	*

$$\frac{S}{N} = \begin{cases}
-10 \cdot log\left(\frac{1}{n} \sum_{i=1}^{n} \frac{1}{y_i^2}\right) LTB \\
-10 \cdot log\left(\frac{1}{n} \sum_{i=1}^{n} y_i^2\right) STB \\
-10 \cdot log\left(\frac{1}{n} \sum_{i=1}^{n} (y_i - m)^2\right) NTB
\end{cases} (7)$$

where n represents the total number of experimental groups,  $y_i$  represents each response objective, and m represents the theoretical value of the response objective.

- (5) Standardized SRN and calculated grey correlation coefficient (GRC)
  - i) Create an initial matrix of SNR:

$$\mathbf{Y}_{mn} = \begin{bmatrix} Y_{11} & Y_{12} & \cdots & Y_{1n} \\ Y_{21} & Y_{22} & \cdots & Y_{2n} \\ \cdots & \cdots & \cdots & \cdots \\ Y_{m1} & Y_{m1} & \cdots & Y_{mn} \end{bmatrix}$$
(8)

where m and n are 16 and 4, respectively.

# ii) Standardized matrix of SNR

Since the raw SNR data of the response objective are often not located on the same scale, it is difficult to make direct comparisons. Therefore, normalization of SNR is required:

$$X_{i}(k) = \begin{cases} \frac{Y_{i}(k) - \min Y_{i}(k)}{\max Y_{i}(k) - \min Y_{i}(k)} & LTB \\ \frac{\max Y_{i}(k) - Y_{i}(k)}{\max Y_{i}(k) - \min Y_{i}(k)} & STB \\ 1 - \frac{|Y_{i}(k) - OB|}{\max \{\max Y_{i}(k) - OB, OB - \min Y_{i}(k)\}} & NTB \end{cases}$$
(9)

where i=1–16, k=1–4,  $Y_i(k)$  is initial  $SNR, X_i(k)$  is normalized SNR, OB is ideal value of  $Y_i(k)$ , and  $X_i(k) \in [0,1]$ . In this study, the SNR conforms to the characteristics of the LTB. The normalized SNR can be represented by the following matrix.

$$\mathbf{X_{nor}} = \begin{bmatrix} X_{11} & X_{12} & \cdots & X_{1n} \\ X_{21} & X_{22} & \cdots & X_{2n} \\ \cdots & \cdots & \cdots & \cdots \\ X_{m1} & X_{m1} & \cdots & X_{mn} \end{bmatrix}$$
(10)

iii) Calculated GRC

The GRC of  $(\zeta_{ij})$  can be calculated by:

$$\zeta_{ij} = \frac{\Delta_{\min} + \omega_{dc} \Delta_{\max}}{\Delta X_{ii} + \omega_{dc} \Delta_{\max}}$$
(11)

where  $\Delta X_{ij} = |X_{oj} - X_{ij}|$ ,  $X_{oj}$  is the ideal value of  $X_i(k)$ , and which is set to 1.0  $\Delta_{\min}$  and  $\Delta_{\max}$  are minimum and maximum values of  $X_i(k)$ ,  $\omega_{dc}$  is the recognition coefficient, which is set to 0.5 in this study.

(6) Calculate the grey correlation (GRG);

The multi-objective optimization can be transformed into single-objective optimization with the help of weighted *GRG*, which can be expressed as:

$$\gamma_i = \sum_{i=1}^n w_i \zeta_{ij} \tag{12}$$

where i = 1–25 and j = 1–5,  $\gamma_i$  denotes the GRG of the  $i_{th}$  set of experiments.

- (7) Carry out an SNR and GRG analysis to obtain an optimized combination of process parameters;
- (8) Conduct experimental validation.

#### 3. Experiments

#### 3.1. Process and characterization of composite coatings

The substrate for the study is 40Cr. As shown in Fig. 1a, TiC ceramics were in situ synthesized by adding pure Ti powder (21.65–148.05  $\mu m$ ) and Ni-coated graphite (26.87–139.88  $\mu m$ ) to improve the resistance of Ni-based high-temperature alloy. The SEM morphologies of In625, pure Ti, and Ni-coated graphite powders can be found in Refs. [5,31]. The chemical composition of In625 and 40Cr is listed in Table 3. A compositional gradient design was carried out to decrease the internal defects of the composite coatings. The content of pure Ti powder and Ni-coated graphite with an atomic ratio of 1:1 is gradually increased with the increase of the number of deposited layers, as shown in Fig. 1a. The experiments were performed on a coaxial laser DED system, and detailed parameters can be are given in Ref [7]. The experimental procedure is shown in Fig. 1b. The optimized process parameters adopted during the experiments are shown in Table 4. The fabricated composite coatings are shown in Fig. 1c.

To evaluate the grinding performance of the composite coatings, the microstructure and mechanical properties of the composite coatings need first to be assessed. The top and cross-section of the composite coating were obtained by wire cutting and subsequently ground by 200 grit to 2000 grit sandpapers. The polished surface was etched in aqua regia for 10 to 30 s to indicate the microstructural details. The elemental content and microstructural characteristics from the bottom to the top were analyzed by scanning electron microscopy (SEM, Zeiss Germany) equipped with an energy dispersive spectrometer (EDS). The microhardness was measured by a Vickers hardness tester (HV-1000, China) with an indentation of 300 gf over a distance of 200  $\mu$ m and a dwell time of 10 s. The wear experiments were conducted on the top of the

composite coating (Fig. 8a) by a multifunctional surface property measuring instrument (MFT-4000, China) with the following parameters: SiN ball with a diameter of 5 mm, time of 60 min, loading force of 15 N, and a distance of 5 mm. The 3D and detailed morphologies of the wear track were obtained by 3D laser microscopy (DSX1000. Japan).

# 3.2. Experiments design and characterization

To analyze the grinding performance of laser DED TiC reinforced composite coatings, as well as to reveal the effects of grinding process parameters on surface roughness and grinding force, typical grinding process parameters were selected as the experimental factors. The sixteen sets of Taguchi-orthogonal experiments were designed, as shown in Table 5. The grinding experimental setup is shown in Fig. 2. The detailed parameters of the grinding wheel are shown in Table 6. Before the grinding experiment, to eliminate the effect of the difference of the initial surfaces on the results, the composite coating was processed for rough grinding. The surface of composite coatings after pretreatment is shown in Fig. 1d. Besides, each set of experiments was repeated twice to reduce the existence of accidental results. During the experiment, the grinding force signals were obtained using a Kistler 9257B force dynamometer equipped with a Kistler 5070 charge amplifier and an A/D data acquisition card. The grinding force signals are transmitted to the computer through amplifiers and converters, as shown in Fig. 2. To accurately collect the grinding force data, the hopping error of the charge amplifier is controlled within the range of 0.005 N/s, the sampling frequency of the A/D data acquisition board is 7000 Hz, and the grinding force measurement range is 0-500 N. The average value of the steady-state grinding signals was taken as the grinding force. The 3D morphologies and surface roughness of the ground surfaces were also measured by 3D laser microscopy, as shown in Fig. 3.

# 4. Results and discussion

# 4.1. Characterization of DED composite coatings

# 4.1.1. Surface morphology analysis

The top surface morphologies of the laser DED composite coating are

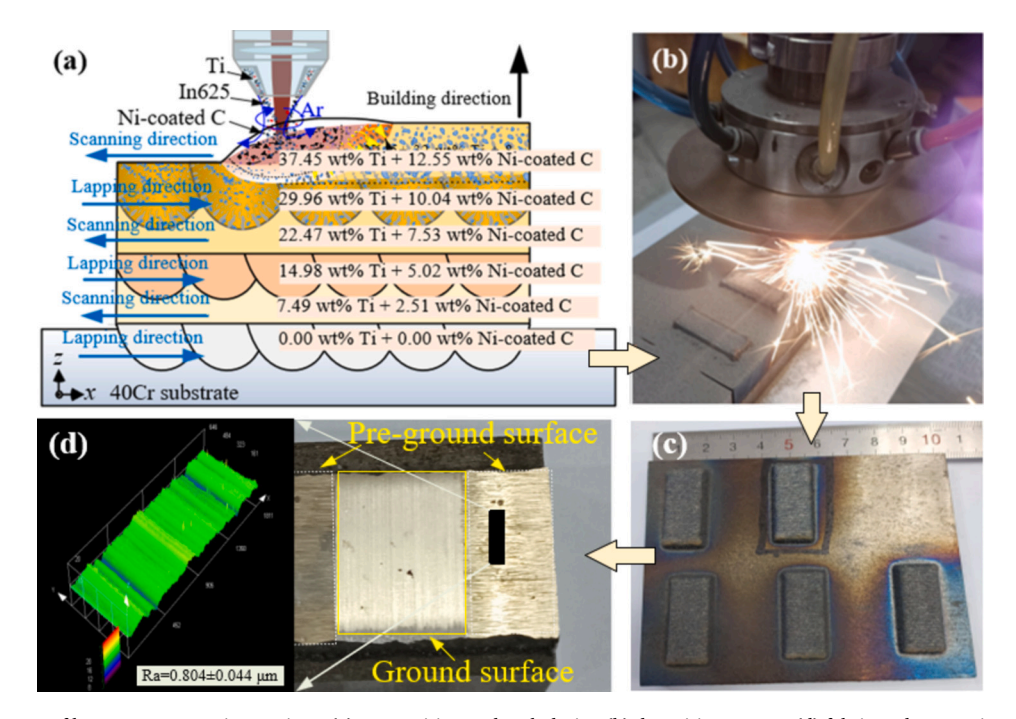


Fig. 1. Fabrication process of laser DED composite coatings: (a) composition and path design (b) deposition process (d) fabricated composite coatings (d) pre-ground surface of the composite coating.

Table 3
Chemical composition of In625 powder and 40Cr substrate (wt%).

	Cr	Мо	Nb	Mn	Si	С	S	P	Ni	Fe
In625	20.0-23.0	8.0-10.0	3.15-4.15	≤0.5	≤0.5	0.02	_	_	Bal.	≤5.0
40Cr	0.80-1.10	< 0.1	_	0.50-0.80	0.17 - 0.37	0.37-0.44	≤0.035	≤0.035	≤0.30	Bal.

**Table 4**Process parameters for laser DED TiC reformed composited coatings.

	Power	Scanning speed	Powder feed rate	Overlapping	Z- increment
YAG	450 W	10.0 mm/s	0.9 r/min	30 %	0.18 mm

**Table 5**Orthogonal table for grinding experiments.

No.	Grinding speed $v_s$ (m/s)	Feed rate $v_{\rm w}$ (m/min)	Cutting depth $a_p$ ( $\mu$ m)
1	10	1	15
2	10	2	30
3	10	3	45
4	10	4	60
5	15	1	30
6	15	2	15
7	15	3	60
8	15	4	45
9	20	1	45
10	20	2	60
11	20	3	15
12	20	4	30
13	25	1	60
14	25	2	45
15	25	3	30
16	25	4	15

shown in Fig. 4. Regular grooves can be found on the top surface of the composite coating. At the same time, some unmelted metal powder can be observed bonded to the surface. The surface roughness of the center area at the top of the composite coating is 10.79  $\pm$  2.33  $\mu m.$  However, the surface roughness of the edge area at the top of the composite coating was significantly increased to 13.15  $\pm$  4.64  $\mu m$ . When the melt pool travels to the center of the composite coating, preheating and heat build-up contribute to increased temperature, resulting in a fuller melting of the metal powder. This behavior effectively decreases the surface roughness. However, when the melt pool travels to the edges of the composite coating, the behavior is reversed, resulting in an insufficient melting of the powder and a significant increase in surface roughness, as shown in Fig. 4b2. As a result, there can be found significant differences in surface quality at different locations of the one composite coating. In addition, a large number of studies [5,11,14] have also found that the effect of surface roughness of composite coatings by

optimizing the laser DED process parameter is not significant. Therefore, this study focuses on the grinding machinability of composite coatings and analyzes the effect of grinding process parameters on the grinding quality. Before the grinding experiments, the composite coatings were pre-treated to avoid the effect of different initial surface morphology on the results of the grinding experiments.

# 4.1.2. Microstructure analysis

The relative contents of Ti, Cr, Fe, and Ni elements were obtained by EDS from the substrate to the top of the in situ TiC-reinforced Ni-based composite coating, as shown in Fig. 5. As deposition height increased, the content of Cr and Ni elements gradually increased. While the content of Fe elements followed the opposite trend. The rich Ni element in the composite powder is fully mixed with the rich Fe element in the substrate under the action of strong Marangoni convection (velocity > 400 mm/s). Therefore, the [Fe—Ni] solid solutions are formed at the bottom of the composite coating. Consequently, Fe elemental content was increased and Ni elemental content was decreased in layer 1 because of the convection in the melt pool. When the content of Ti and Ni-coated C exceeded 30 wt% (deposition height  $> 1800 \mu m$ ), the content and size of in situ synthesized TiC exceeded 2.20 µm and 25.00 %, respectively, as shown in Fig. 6. At this point, the in situ synthesized ceramic particles are coarse enough to be detected by EDS. Therefore, the position of the Ti elemental peak corresponds to the TiC ceramics. It was found that in situ synthesized TiC tends to aggregate at the top of the melt pool due to the lower density (4.93 g·cm<sup>-3</sup>) [32,33]. However, it can be noticed from Fig. 5 that the trend of Ti content in the composite coatings is very smooth as the deposition height increases. On the one hand, the chemically active Ti elements are susceptible to the formation of TiO2 and TiN with  $O_2$  and  $N_2$  in air [34,35]. Since the solidification time of the melt pool is very short (< 0.085 s), these titanium compounds do not have enough time to escape from multi-phase liquids and are retained at the top of the melt pool. During subsequent deposition, these titanium compounds are reabsorbed and decomposed. Thereby, the content of in situ synthesized TiC at the bottom of the melt pool is increased. On the other hand, since the exposure area between the Ti element and the air at the top of the melt pool is larger, the oxidation of the Ti particles is

**Table 6**Parameters of the cBN grinding wheel.

Abrasive	Mesh	Diameter	Thickness	Width
cBN	200#	80 mm	10 mm	15 mm

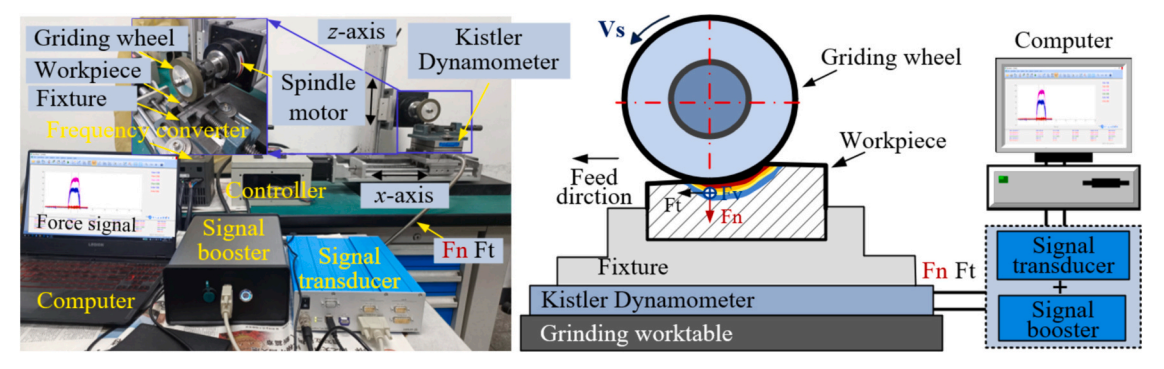


Fig. 2. Experimental setup and schematic diagram of grinding force.

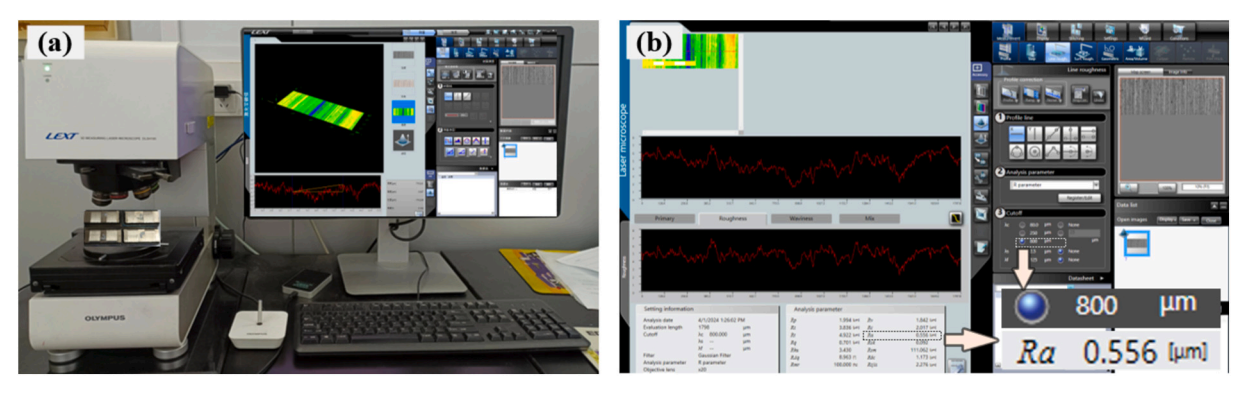


Fig. 3. The process of obtaining surface roughness: (a) laser confocal microscopy, (b) roughness measurement.

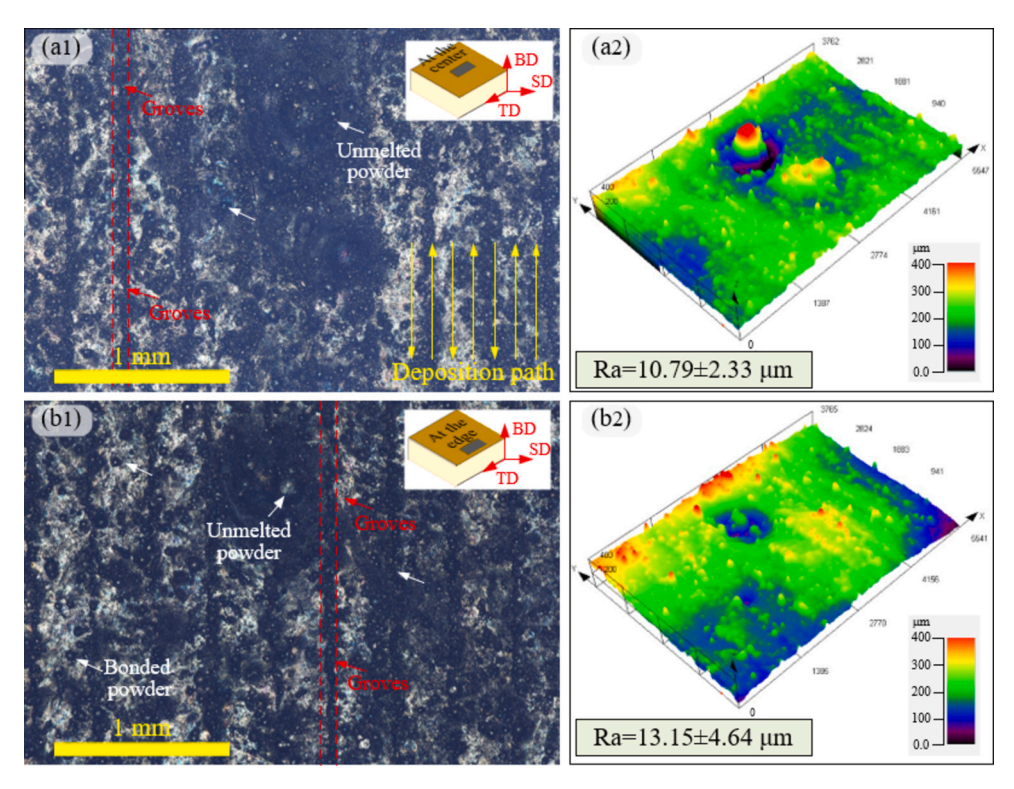


Fig. 4. Top surface morphology of composite coating: (a) at the center and (b) at the edge.

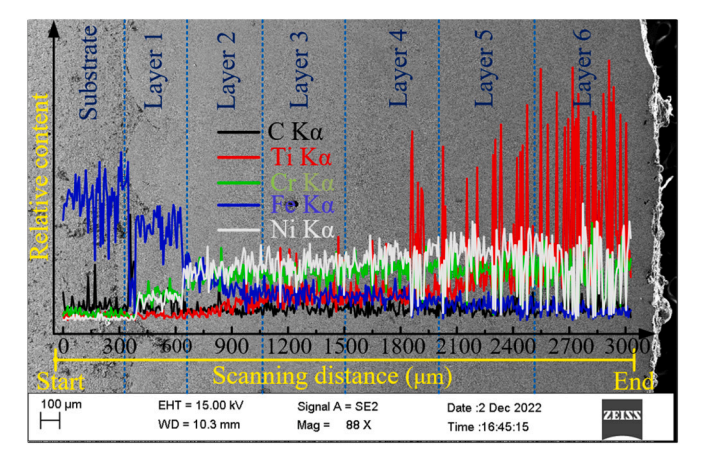


Fig. 5. Variation of elemental content of the TiC-reinforced Ni-based composite coating.

more intensive. The TiC content has been slightly decreased. Above, all, the oxidation is favorable for the gradient distribution of in situ TiC in the composite coating during the deposition process. In addition, since the density of NbC (8.47 g·cm³) is larger than that of TiC ceramics [35], the upliftment of TiC ceramics can be effectively decreased due to formation of multi-ceramic (Ti, Nb)C. which promotes the homogeneous transition of microstructure and elemental distribution composite coatings. This behavior can promote a uniform transition in the microstructure and elemental distribution of the composite coating.

The optical microstructure and locally enlarged SEM morphology of the composite coatings are shown in Fig. 6. The microstructure is significantly changed with the increase of deposition height. The clearly defined bond lines in Fig. 6 demonstrate a good metallurgical bond between the coatings and substrate. Fig. 6a shows that the bottom of the composite coating is composed of coarse columnar grains. However, when the addition of Ti and Ni-coated C is 10 wt%, the bottom of layer 2 is dominated by fine equiaxed grains, as shown in Fig. 6b. This suggests that in situ synthesized fine ceramic particles can refine the grains and promote the columnar to equiaxed transformation. When the content of Ti and Ni-coated C exceeded 30 wt%, in situ coarse TiC particles are

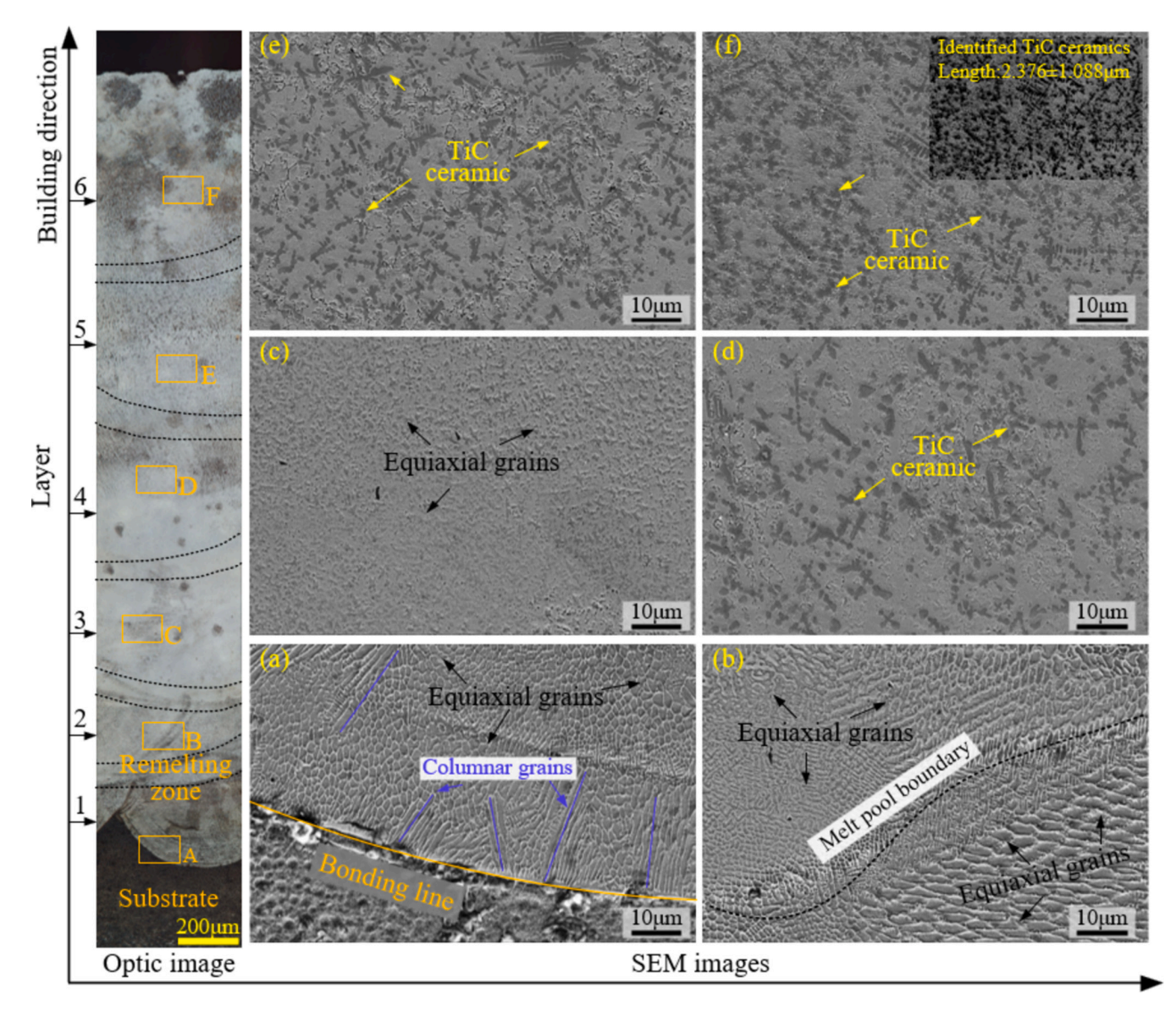


Fig. 6. SEM images of the TiC-reinforced Ni-based composite coating.

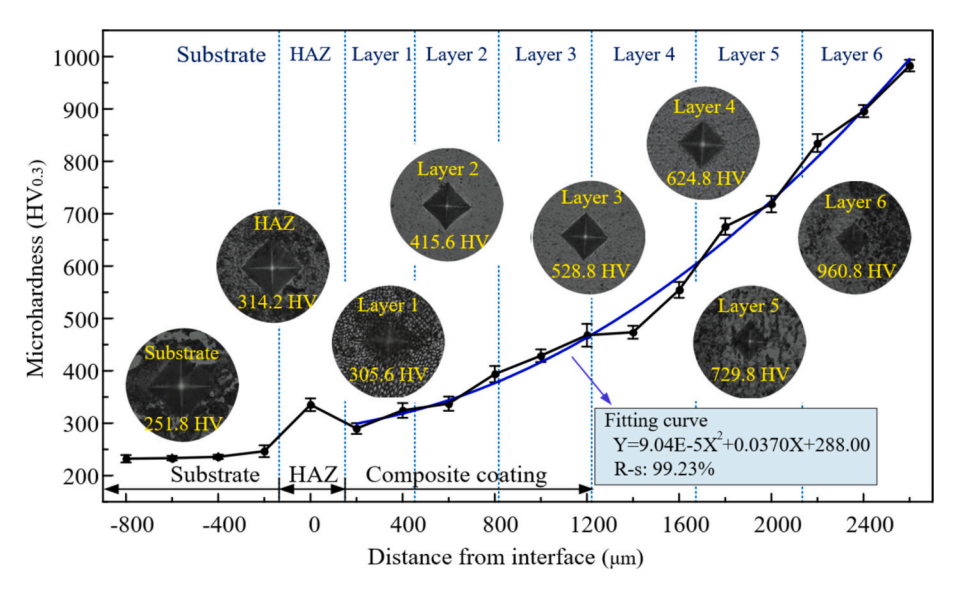


Fig. 7. Microhardness distribution and indentation morphologies of composition coating.

found at the top of layer 4. The localized Ti elemental content was increased, as shown in Fig. 6d. As a result of the layer-by-layer buildup of LDED, the microstructure within the remelted zone is different from that within the deposited layer [36]. This phenomenon is prone to result in differences in mechanical properties of hardness, wear resistance, and tensile strength [37]. However, it can be found from Fig. 6e and f that the grain morphologies at the melt pool between layers 5 and 6 are nearly identical. As a result, the remelting zone of the composite coating decreased and disappeared with increasing height. The anisotropy of the composite coating was significantly weakened [38].

# 4.1.3. Performance analysis

The microhardness variation from the bottom to the top of the composite coating is shown in Fig. 7. The microstructure around the indentation reveals the effect of the content and size of the in situ synthesized TiC on the microhardness. Microhardness gradually increased from the lowest value (330.87  $HV_{0.3}$ ) at the bottom to the maximum value (939.35 HV<sub>0.3</sub>) at the top along the building direction. The relationship between microhardness (Y) and deposition height (X, µm) satisfies: $Y = (9.04E - 5) \cdot X^2 + 0.0370 \cdot X + 288.00$  with a regression coefficient of 99.23 %. Compared to the composite coatings fabricated by direct addition methods, in situ TiC reinforced Ni composite coatings exhibit a smoother transition to microhardness [37,39]. On the one hand, the in situ synthesized TiC ceramics with high microhardness act as a particle load-bearing reinforcement. The deformation resistance was improved. On the other hand, in situ TiC particles can decrease the temperature gradient at the solidification front, decrease the direction of the heat flow density, inhibit the formation of columnar crystals, and refine the equiaxial crystals. The fine-grain reinforcement of the matrix can be realized. In addition, the high concentration of Ti and C elements at the top of the pool flows to the bottom of the pool under the effect of positive surface tension coefficients. During the rapid solidification process, the fine TiC particles are retained in the crystal cells, which play a role in solid solution strengthening. As a result, the variability of the microstructure between the layers is gradually decreased, which promotes the uniform transmission of the stresses and strains. In summary, the internal defects of in situ synthesized ceramic reinforced composite coatings are significantly decreased, and the transition of microstructure and mechanical properties at the melt pool boundary is smoother.

To analyze the grinding removal model of ceramics and matrix of composite coating, the friction coefficient, 3D morphology of the worn surface, and cross-sectional profile are obtained, as shown in Fig. 8.

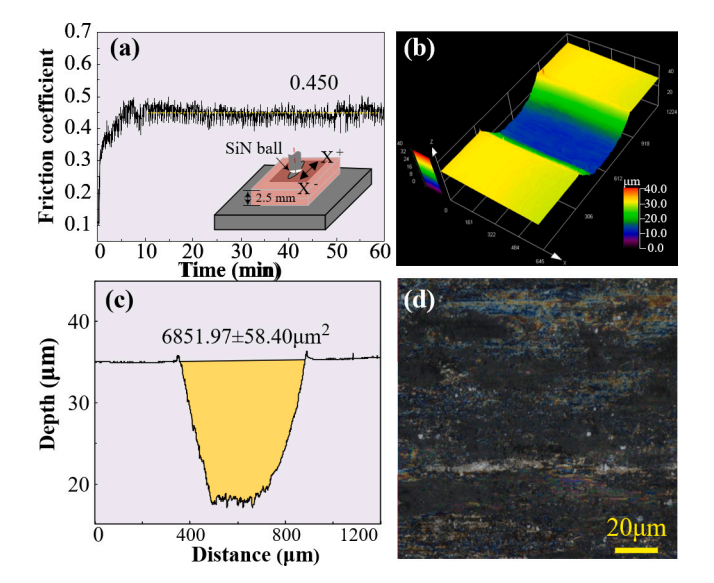


**Fig. 8.** Wear performance of the TiC reinforced Ni-based composite coating: (a) friction coefficient, (b) 3D surfaces, (c) sectional profile (d) worn surface.

According to the variation of friction coefficient (Fig. 8a), the whole wear process can be divided into initial and stable wear stage. During the initial break-in stage, the contact area between the worn surface and the SiN ball is small because little material has been removed from the sample surface. As the wear progresses, the surface material is gradually removed by the greater stress. The contact area of the friction pair becomes larger and the wear process stabilizes. After about 15 min, the friction coefficient stabilized and the steady friction stage was reached.

To deeply reveal the wear characteristics, wear surface 3D and crosssection profiles were obtained (Fig. 8b and c). The internal residual stresses in laser DED coatings are often significant and the distribution is usually regional [40]. The spalling of the material from the worn surface is easy to occur under the repeated action of the friction partner. In addition, the lower speed movement of the friction pair (220 mm/min) allows the tough abrasive chips to adhere to the surface of the grinding balls. The resistance was increased. The large number of uniformly distributed ceramic particles act as a skeleton to carry the load during wear, decreasing the detachment of the matrix with low hardness, as shown in Fig. 8d [41]. In addition, the ceramic phase removed by microcutting acts as a lubricant during the wear process. The friction coefficient was decreased and the smoothness of the worn surface was improved. However, when the composite coatings are subjected to multiple cyclic stresses, a small amount of surface material is partially stripped and small pits are formed, exhibiting abrasive and adhesive wear characteristics [31,42].

# 4.2. Grinding surface morphologies analysis

During the grinding process of composite materials, the microcontact state between abrasive grains and different locations of the sample mainly includes three stages of scratching, plowing, and chip formation. The remove characteristics can be divided into toughness or brittleness mode [43,44]. To comprehensively analyze the grinding performance of composite coatings, this study adopted cutting depth  $(a_n)$  as the main criterion. The larger machining parameters of samples No.1, 12, 14, and 7 were selected as the comparative analysis. Optical images, 3D morphologies, and cross-sectional profiles of ground surfaces are shown in Fig. 9. Along the grinding direction, the ground surface is dominated by continuous plow-like grooves, which are typical of plastic deformation. It can be noticed that the ground surface of sample No.1 is characterized by significant toughness removal. However, some pits and a small amount of grain chips are also present on the ground surface. Numerous studies [27,45] have found that hard and brittle TiC ceramics are mainly cut and extracted during the grinding process. Some chips are attached to the ground surface and provide a certain lubrication effect, which is beneficial for improving the surface quality. Besides, the soft matrix of Ni is removed in a toughness model, resulting in plow-like pits. As the cutting depth increases, the width and depth of the plow-like grooves gradually increase. This phenomenon is not conducive to improving the ground surface quality of the composite coating, as shown in Fig. 9d.

To reveal the ground surface morphologies of the composite coating in more detail, optical images of the ground surfaces are obtained, as shown in Fig. 10. Compared to ground surfaces of ceramic reinforced composites [46,47], the number and size of pits formed by brittle spalling are significantly decreased. While the ground surface of the composite coating is mainly distributed in continuous plow-like grooves. This phenomenon can effectively improve surface quality and avoid grinding burns and subsurface damage. On the one hand, the bonding strength of the in situ synthesized ceramic particles to the matrix is significantly improved [48,49]. As a result, the flaking of ceramic particles is significantly decreased during the grinding process [36,50]. On the other hand, the length of the in situ synthesized ceramic particles is only 2.376  $\mu m$ , as shown in Fig. 6f. Although the microhardness of the composite coating is as high as 1000 HV, smaller ceramic particles can be removed integrally with the tough matrix of Ni under the action of

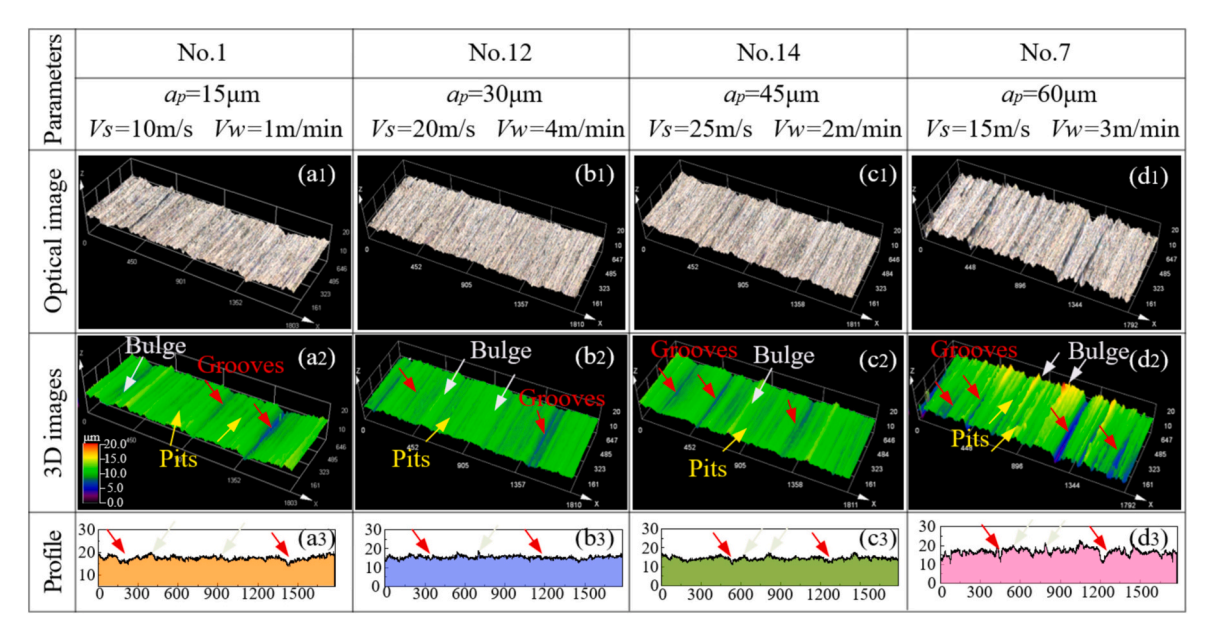


Fig. 9. Ground surface morphologies of laser DED TiC reinforced composite coating.

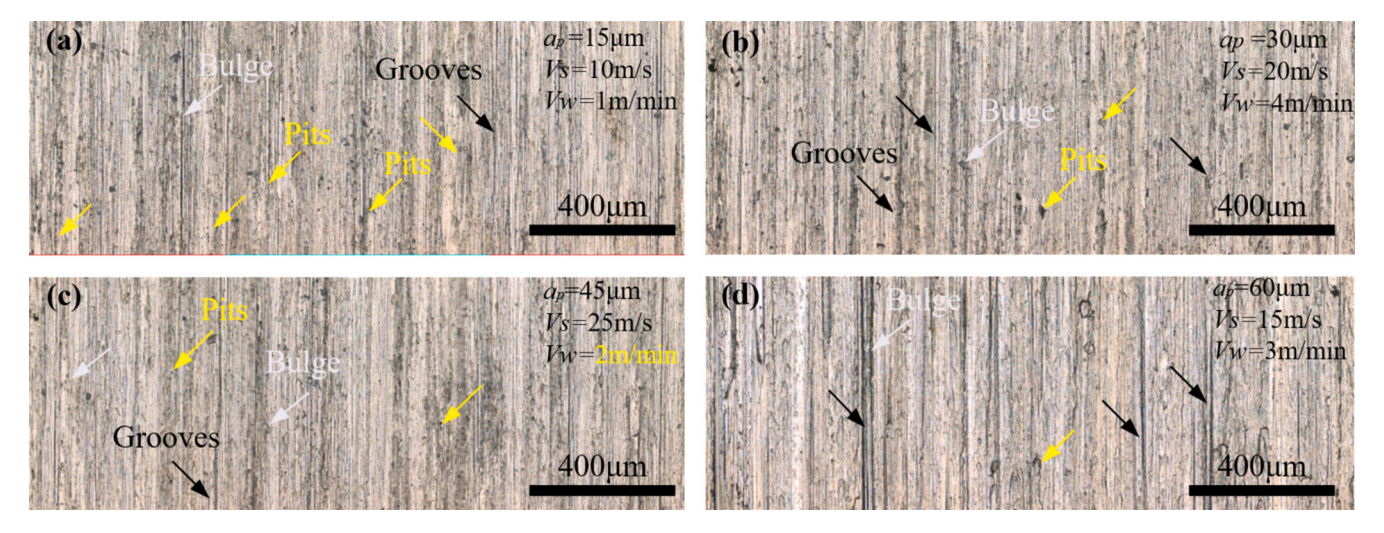


Fig. 10. Optical images of ground surfaces: (a) Sample No.1, (b) Sample No.12, (c) Sample No.17, and (d) Sample No.7.

cBN [7,22]. Therefore, the breakage of ceramic particles is significantly decreased and the number of plow-like grooves is significantly increased. However, as the cutting depth increases, the prominence of hard particles and the depth of grooves formed by the removal of the tough matrix also increase significantly, as shown in Fig. 10d.

# 4.3. Grinding force signals analysis

The variation of force signals during the grinding process is closely related to the rigidity of machining accuracy, chatter, grinding wheel wear, and the process parameters [51]. Therefore, grinding force is an important parameter for characterizing material removal mode and machined surface [52,20]. The force signals of samples No.1, 12, 14, and 7 are obtained, and the results are shown in Fig. 11. The normal force  $(F_n)$  and tangential force  $(F_t)$  undergo three phases of rapid rise, steady, and decrease. The dwell time of stabilization is inversely proportional to the feed rate. To reduce the effect of the instability stage, the average grinding force at the steady phase is taken as the grinding force in this study. It is worth noting that the tangential force  $(F_t)$  is about 0.5 times the normal force  $(F_n)$ , which is the same as previous studies [53,27]. The

enlarged tangential force (*Ft*) in Fig. 11 reveals that the force signal is subject to unstable fluctuations, which might result in damage on the ground surface [23]. The fluctuations could be attributed to differences in the form of material removal on the ground surface. In addition, the ceramic particles would be subjected to impact and shearing by cBN abrasive grains during the grinding process. When these forces exceed the fracture strength of TiC ceramics, the ceramic particles are momentarily touched or cut off, which also results in a variation of the grinding force signals [15]. Moreover, the sudden increase in grinding force for brittle ceramic particles is typically 5 to 10 % of that under plastic removal, which can result in fluctuations in the grinding force signal [54].

# 4.4. Optimization of grinding process parameters

# 4.4.1. The effect of process parameters on grinding characteristics

The surface roughness (Ra) and grinding force of each sample are shown in Fig. 12. It can be found that the variation rule of surface roughness (Ra) and grinding force is consistent. When the grinding wheel cBN grits are in contact with the composite coating, more ceramic

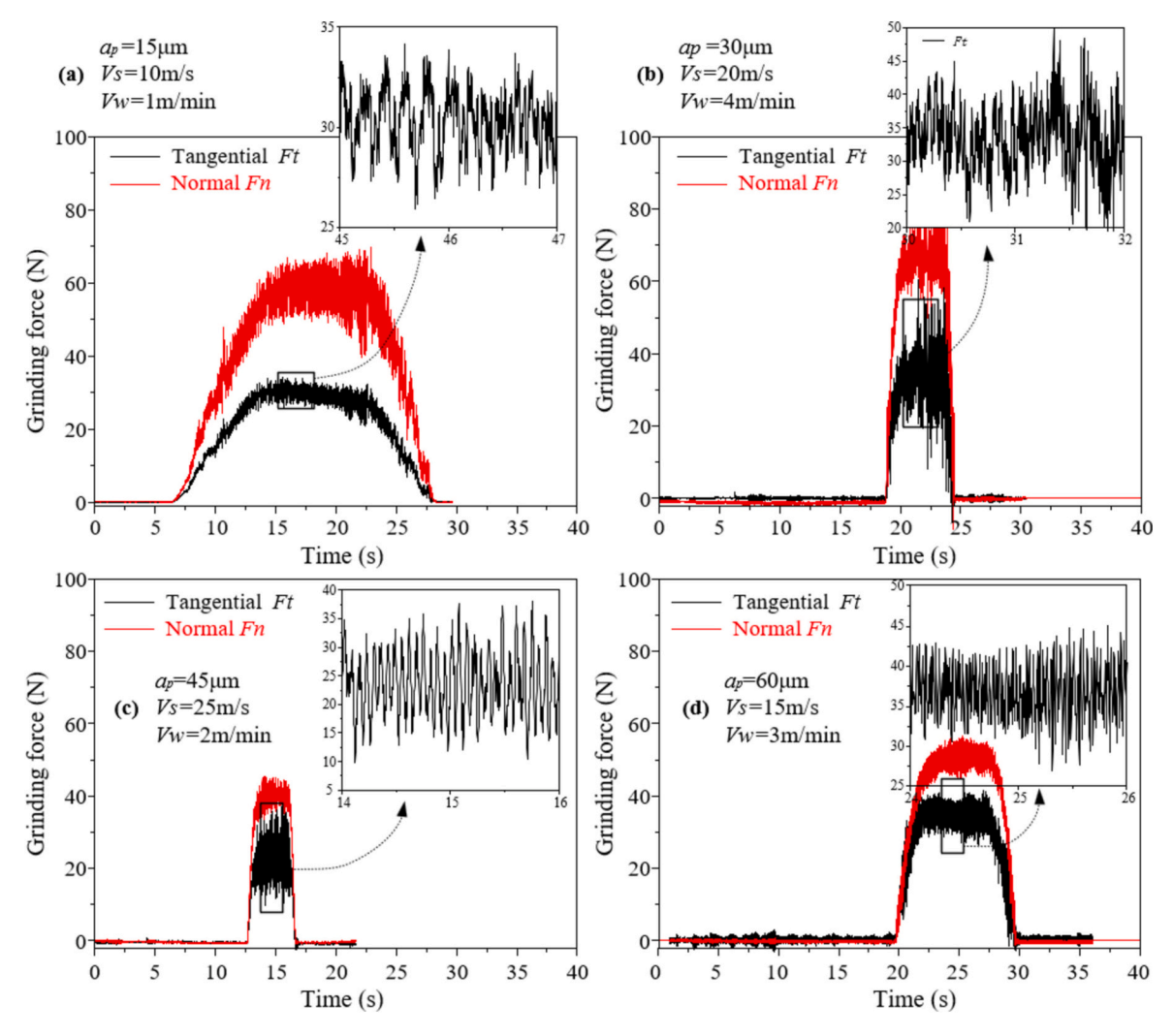


Fig. 11. Grinding force signals during the grinding process: (a) Sample No.1, (b) Sample No.12, (c) Sample No.17, and (d) Sample No.7.

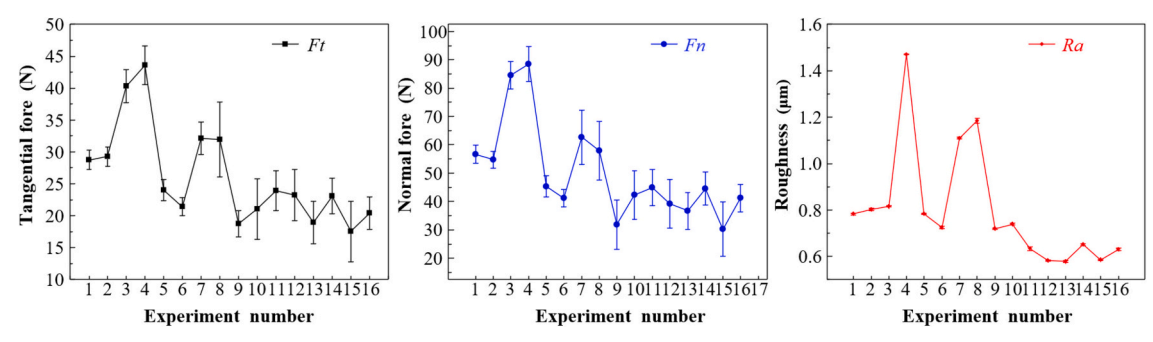


Fig. 12. Measured results of roughness and grinding force on TiC reinforced Ni-based composite coatings.

particles are plucked, cut off, and removed by the plowing of the tough matrix. At the same time, the surface roughness increases significantly. It is also found from Fig. 12 that the grinding force and surface roughness of the composite coating decrease gradually with the increase in grinding speed. Whereas, when the speed is the same, the grinding force and surface roughness of the composite coating increases with the increase in feed rate and cutting depth.

To analyze the effect of process parameters on the response objective, the surface roughness and grinding force (Fig. 12) were subjected to ANOVA according to Eqs. (1)–(6). The results are shown in Table 7. It can be found through Table 7 that the contribution of  $\mathbf{v}_s$ ,  $\mathbf{v}_w$ , and  $a_p$  to the

Ra is 69.63 %, 17.33 %, and 13.04 % respectively. Therefore,  $v_s$  can be regarded as an important factor in determining the surface roughness. According to the joint hypothesis test (F-test), it can be obtained  $F_{0.01}(3, 6) = 9.7795$ , and  $F_{0.05}(3, 6) = 4.76$  [55]. Combined with the ANOVA of Ra (Table 6), it can be found that  $F(Ra) > F_{0.05}(3, 6)$ , which indicates that the grinding speed exerts a significant effect on the surface roughness.

The effect of process parameters on the mean values of grinding forces (Ft and Fn) and surface roughness are shown in Table 8 and Fig. 13. When  $v_s$  increases from 10 m/s to 25 m/s, the surface roughness of the ground surface gradually decreases from 0.97  $\mu$ m to 0.36  $\mu$ m. As

**Table 7**ANOVA results for grinding characteristics.

Source		Grinding speed v <sub>s</sub> (m/s)	Feed rate $v_{\rm w}$ (m/min)	Cutting depth $a_{\rm p}$ ( $\mu$ m)	Residual error	Total
	Freedom degrees	3	3	3	6	15
	Seq. SS	0.4143	0.1598	0.2244	0.1315	0.93
Roughness	Adj. MS	0.13809	0.05326	0.07481	0.02192	
Ra	F	6.30	2.43	3.41		
	P	0.028	0.163	0.094		
	Contribution	51.89 %	20.02 %	28.09 %		
	Freedom degrees	3	3	3	6	15
	Seq. SS	583.89	145.34	109.31	41.83	880.37
Tangential force	Adj. MS	194.63	48.447	36.437	6.972	
Ft	F	27.92	6.95	5.23		
	P	0.001	0.022	0.041		
	Contribution	69.63 %	17.33 %	13.04 %		
	Freedom degrees	3	3	3	6	15
	Seq. SS	2788.8	595.5	597.9	286.7	4268.8
Normal force	Adj. MS	929.59	198.48	199.3	47.78	
Fn	F	19.46	4.15	4.17		
	P	0.002	0.065	0.065		
	Contribution	70.05 %	14.94 %	15.01 %		

**Table 8**Optimize the mean value of the response objective.

Levels	Roughness	(Ra)		Tangential force (Ft)			Normal force (Fn)		
	$v_s$	$\nu_{ m w}$	$a_p$	$v_s$	$\nu_{ m w}$	$a_p$	$v_s$	$\nu_{ m w}$	$a_p$
1	0.97	0.72	0.70	35.48	22.61	23.63	71.12	42.63	46.02
2	0.95	0.73	0.69	27.37	23.70	23.51	51.79	45.72	42.39
3	0.67	0.79	0.84	21.73	29.29	29.34	39.58	56.6	55.71
4	0.61	0.97	0.97	19.99	28.97	28.10	38.19	55.73	56.57
Delta	0.36	0.25	0.29	15.49	6.68	5.83	32.93	13.97	14.19
Rank	1	3	2	1	2	3	1	3	2

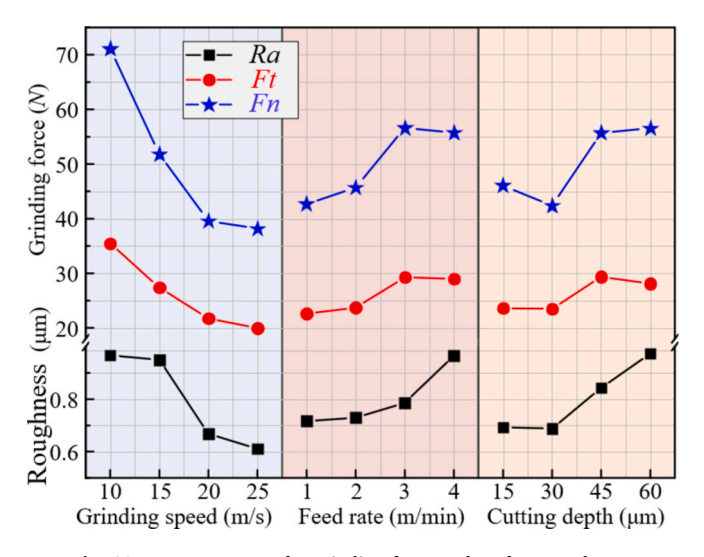


Fig. 13. Mean response for grinding force and surface roughness.

the grinding speed increases, the number of abrasive grains engaged in grinding per unit of time increases [27]. The thickness of the undeformed chip layer was decreased [45]. As a result, the height between the peaks and valleys on the ground surface is significantly decreased, resulting in a smaller Ra. In addition, brittle ceramic particles are broken and dislodged from the surface by the impact and extrusion of the grinding wheel during the grinding process. These fracture and flaking areas are not flat. However, as the speed of the grinding wheel increases, the relative velocity between the abrasive and ceramic particles increases significantly. Under the effect of large impacts, the ceramic particles would be removed by more cut-off. Therefore, the surface

roughness of the ground surface can be increased [56]. As the feed rate increased from 1 m/min to 4 m/min and the cutting depth increased from 15  $\mu m$  to 60  $\mu m$ , the surface roughness Ra gradually increased from 0.72  $\mu m$  to 0.97  $\mu m$ , as shown in Fig. 13. On the one hand, with the increase in feed rate and cutting depth, the thickness of the undeformed cutting layer of a single grain increases significantly. As a result, the transformation of localized hard and brittle ceramic particles from plastic to brittle removal can appear. On the other hand, a significant increase in grinding size accompanies the increase in material removal rate. The abrasive removal process can also become difficult. In addition, as the grinding depth increases, the grinding force and grinding heat are significantly improved. As a result, ground surface burns and sub-surface damage would significantly increase, resulting in poor ground surface quality.

It can be found from Fig. 13 that the degree of effect of process parameters on tangential force and normal force is almost the same. Therefore, the Ft is taken as the main object of analysis in this study. It can be found from Table 7 that the contribution of  $v_s$ ,  $v_w$ , and  $a_p$  to the Ft is 69.63 %, 17.33 %, and 13.04 % respectively. In addition,  $F(v_s)$  >  $F_{0.01}(3, 6), F(v_w) > F_{0.05}(3, 6), \text{ and } F(a_p) > F_{0.05}(3, 6).$  Therefore,  $v_s, v_w$ and  $a_p$  all have a highly significant effect on the Ft. According to Table 8, it can be found that the main order of effect of process parameters on Ft is  $v_s > v_w > a_p$ . As shown in Fig. 13, as the grinding speed increases from 10 mm/s to 25 mm/s, Ft decreases gradually from 35.48 N to 15.49 N and normal grinding force decreases gradually from 71.12 N to 32.93 N. As the grinding speed increases, the number of abrasive grains per unit of time involved in grinding increases. This phenomenon decreases the time between abrasive grains and the ground surface. The thickness of the undeformed cutting layer is decreased. In addition, when the grinding speed is sufficiently high to exceed the rate of plastic deformation transmission, the material is removed without deformation. As a result, a large amount of heat is carried away with the grinding chips. The wheel clogging and grinding forces were decreased. As the feed rate

and cutting depth increase, the tangential grinding force first increases and then decreases. The length of the contact arc between a single grain and the ground surface was increased. Moreover, the thickness of the undeformed cutting layer also increased. Although the grinding removal efficiency can be improved, the grinding force and surface roughness would be greatly increased. Therefore, the feed rate and cutting depth can be appropriately decreased to reduce the grinding force.

# 4.4.2. Optimization process and experimental verification

Surface roughness is an important parameter in assessing machining accuracy, and it is generally accepted that lower cutting forces result in better-machined surface quality [26]. Therefore, the response objectives were selected as surface roughness (Ra) and grinding forces (Fn and Ft) in this study. The grinding forces are desired to be smaller to reduce subsurface damage. Therefore, the response targets (Ra, Fn, and Ft) satisfy the expected smallness. The results of the mean SNR of the response objective according to Eq. (9) are shown in Table 9.

The main effect curves of SNR are shown in Fig. 14. As the grinding speed increases, the mean SNR of the surface roughness gradually increases. However, the SNR of the grinding force gradually decreases with increasing feed rate and cutting depth. For the desired low roughness and small grinding forces, the optimal combination of process parameters for the response objective is the same as  $v_s 4v_w 1a_p 2$ . The detailed parameters are a grinding speed of 25 m/s (level 4), a feed rate of 1 m/s (level 1), and a cutting depth of 30  $\mu$ m (level 2), as shown in Fig. 14.

The normalized SNR and GRC were obtained according to Eqs. (10) to (11), as shown in Table 10. The highest grey correlation of 0.991 is found for sample No.15, which corresponds to the grinding process parameters of  $v_s 4v_w 2a_p 3$ . The detailed parameters are a grinding speed of 25 mm/s, a feed rate of 2 m/min, and a cutting depth of 45  $\mu$ m.

By analyzing the SNR of GRG, the main effect curves of the grey correlation are shown in Table 11 and Fig. 15. The optimized combination of grinding parameters is obtained as  $v_s 4v_w 1a_p 2$ . However, the ideal process parameter is not within the orthogonal process parameters of Table 4. Therefore, supplemental experiments were carried out to verify the reasonableness of the process parameter optimization, and the results are shown in Table 12. It can be found that the surface roughness decreased from 0.585  $\mu m$  to 0.543  $\mu m$  with a decrease of 7.18 %. The tangential grinding forces were decreased from 17.53 N to 16.78 N and 29.56 with a decrease of 4.28 %. The normal grinding forces were decreased from 30.27 N to 29.56 N with a decrease of 2.35 %. Previous studies [11,5] have found that the surface roughness (Ra) of composite coatings fabricated by ultrasonic vibratory or ultrahigh-speed laser additive manufacturing is still as high as 12.00 µm. Moreover, the surface roughness (Ra) of the coating fabricated by high-precision SLM additive manufacturing technology also exceeds 4.00 µm [12]. In addition, the surface roughness (Ra) of the composite coating ground using traditional micro grinding is also as high as 1.2 µm because of the lower grinding speed of 2.83 m/s [21]. It is worth noting that the minimum surface roughness (Ra) of the ground surface of the composite coating is 0.543 µm, as shown in Table 12. Compared with previous studies [11,12,21], the surface roughness of the ground composite coating in this study was decreased by 95.48 %, 86.43 %, and 54.75 %,

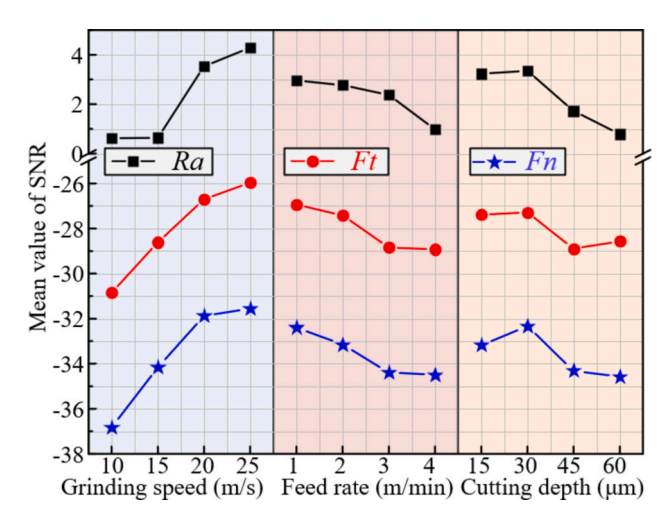


Fig. 14. Main effect curves of the mean SNR for the objective.

respectively. Although the surface roughness (Ra) of the ground laser DED composite coating can be significantly reduced to 0.25 µm by ultrahigh speed grinding [23], the linear velocity of the grinding speed is as high as 130 m/s, resulting in greater energy consumption. However, when the grinding speed is 17 m/s, the surface roughness (Ra) of the ground composite coating is still as high as 0.67 µm [23]. In summary, the Taguchi orthogonal experiment and grey correlation method proposed in this study to optimize the grinding process parameters of laser DED composite coatings are effective and feasible methods for improving the surface quality of composite coatings.

The optical images, 3D and SEM morphologies of the ground surface for the validation experiment are shown in Fig. 16. Compared to the process combination ( $v_s 4 v_w 2 a_p 3$ ), the surface defects (pits) are improved by the process combination of  $v_s 4 v_w 1 a_p 2$ , and the depth of the plow-like grooves is significantly decreased (Fig. 16b2). By comparing the SEM images (Fig. 16 a3 and b3) of the ground surface, most of the ceramic particles are removed by cut-off or extruded into the metal matrix rather than fractured or gouged out to form irregular pits. Therefore, the surface roughness was effectively decreased and the surface quality of the ground surface was improved. Above all, the response objective (surface roughness and grinding force) of laser DED ceramic reinforced composite coatings can be significantly improved using optimized grinding process parameters.

SEM images and the corresponding elemental distributions of the ground surface are shown in Fig. 17. It can be found that all the in situ synthesized TiC ceramic particles are extruded into the soft and tough matrix under the action of normal grinding force. Moreover, no significant interfacial gap is found between the ceramic particles and the matrix. At the same time, the continuous bump was created by the abrasive particles of the grinding wheel in the soft and tough matrix. As shown in Fig. 17b, c, and d, the black ceramic particles are rich in Ti, Nb, C, and Mo elements. This indicates that the in situ synthesized ceramic particles are mainly composed of TiC, NbC, or (Ti, Nb)C. While these ceramic particles were efficiently generated by the catalytic action of the

**Table 9**Mean of SNR for surface roughness and grinding force.

Level	Roughness	s (Ra)		Tangential for	rce (Ft)		Normal force	(Fn)	
	$v_s$	$ u_{\mathrm{w}}$	$a_{\rm p}$	$\overline{\mathbf{v}_{s}}$	$ u_{ m w}$	$a_{ m p}$	$v_s$	$v_{ m w}$	$a_{\rm p}$
1	0.62	2.96	3.23	-30.85	-26.94	-27.39	-36.83	-32.39	-33.18
2	0.64	2.77	3.35	-28.61	-27.42	-27.28	-34.16	-33.15	-32.34
3	3.54	2.38	1.72	-26.7	-28.84	-28.90	-31.88	-34.39	-34.31
4	4.29	0.98	0.79	-25.97	-28.93	-28.56	-31.55	-34.49	-34.58
Delta	3.67	1.99	2.56	4.88	1.98	1.62	5.28	2.11	2.23
Rank	1	3	2	1	2	3	1	3	2

Table 10
Normalized SNR, grey correlation coefficient, and grey correlation for response objectives.

No.	Normalizatio	n of S/N ratio		Grey relation	al coefficient		Grey relationa	al grade
	Ra	Ft	Fn	Ra	Ft	Fn	Values	Rank
1	0.517	0.457	0.416	0.606	0.479	0.461	0.515	11
2	0.441	0.438	0.447	0.587	0.471	0.475	0.511	12
3	0.352	0.000	0.000	0.576	0.333	0.333	0.414	15
4	0.000	0.086	0.043	0.333	0.354	0.343	0.343	16
5	0.766	0.655	0.624	0.606	0.591	0.571	0.589	10
6	0.800	0.780	0.712	0.674	0.694	0.635	0.668	7
7	0.268	0.336	0.321	0.417	0.429	0.424	0.424	14
8	0.355	0.341	0.395	0.394	0.432	0.453	0.426	13
9	0.800	0.927	0.953	0.679	0.873	0.913	0.822	3
10	0.830	0.799	0.687	0.655	0.713	0.615	0.661	9
11	0.775	0.659	0.632	0.837	0.594	0.576	0.669	6
12	0.792	0.691	0.760	0.987	0.618	0.675	0.760	4
13	0.948	0.915	0.821	1.000	0.855	0.736	0.864	2
14	0.870	0.698	0.640	0.798	0.623	0.581	0.667	8
15	0.861	1.000	1.000	0.974	1.000	1.000	0.991	1
16	1.000	0.833	0.711	0.843	0.750	0.634	0.742	5

Table 11 Mean SNR for GRG.

Level	Grey relational grade		
	Grinding speed Vs	Feed rate Vw	Cutting depth ap
1	0.417	0.691	0.645
2	0.539	0.628	0.671
3	0.703	0.584	0.577
4	0.805	0.561	0.572
Delta	0.389	0.130	0.099
Rank	1	2	3

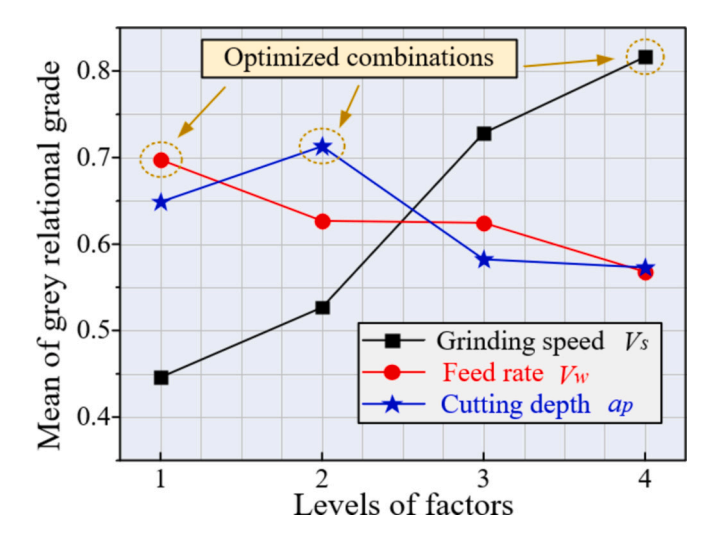


Fig. 15. Main effects curves for mean grey correlation of SNR.

**Table 12** Results of validation experiments.

	Griding parameter co	ombination	Enhancement
	Maximum GRG of No.15	Optimized of $v_s 4v_w 1a_p 2$	ratio
Roughness (Ra)	0.585	0.543	7.18 %
Tangential force (Ft)	17.53	16.78	4.28 %
Normal force (Fn)	30.27	29.56	2.35 %

Mo element. In addition, it can be found from Fig. 17b that abundant Nb elements are distributed around the edges of the ceramic particles. This is similar to the study of Zhao et al. [35], which suggests that (Ti, Nb)C was synthesized in situ at the edges of coarse ceramic particles. Since TiC and NbC have the same lattice constant, Nb and Ti atoms can be exchanged with each other to form (Ti, Nb)C [57,58]. This behavior effectively improves the bonding strength of the coarse TiC ceramics with the matrix and decreases the pulling out of ceramic particles during the grinding process. Therefore, no microscopic cracks, brittle spalling, or fracture-forming pits are found on the ground surfaces, despite the large difference in the modulus of elasticity between the TiC and the Ni alloy. Above all, the ceramic particles and the matrix are removed in a tough mode, which suggests that laser DED in situ ceramic-reinforced Ni-based composite coatings exhibit good machinability.

# 5. Conclusion

In response to the poor surface quality of laser DED in situ synthesized ceramic reinforced composite coatings, the microstructure, mechanical properties, and grinding performance of composite coatings are first investigated in this study. Then, multi-objective optimization of the grinding process parameters for composite coatings is carried out with the help of analysis of ANOVA and grey correlation analysis. The main conclusions are as follows:

- (1) A good metallurgical bonding is generated between the in situ synthesized ceramic particles and the matrix. The relationship between the microhardness (Y,  $_{\rm HV0.3}$ ) and the deposition height (X,  $\mu$ m) satisfies Y = (9.04E 5)· $X^2$  + 0.0370·X + 288.00 with a regression coefficient of 99.23 %. The friction coefficient of the composite coating is 0.45, and the material removal is dominated by abrasive wear and fatigue spalling.
- (2) Signal-to-noise ratio and ANOVA show that the order of effect of process parameters on surface roughness Ra is as follows: vs>ap>vw. The tangential force Ft in the following order: vs>vw>ap. As the grinding speed increases, the surface roughness gradually decreases from 0.97  $\mu$ m to 0.36  $\mu$ m, and the tangential force gradually decreases from 35.48 N to 15.49 N. The decrease in the undeformed cutting layer thickness results in a reduction of surface roughness and grinding forces.
- (3) Based on Taguchi and grey correlation optimization analysis, the optimized grinding process parameters for laser DED ceramic reinforced composite coatings were a grinding speed of 25 m/s, feed rate of 1 m/s, and cutting depth of 30 μm. The surface roughness of 0.543 μm, tangential grinding forces of 16.78 N, and normal grinding forces of 29.56 N using the optimized girding

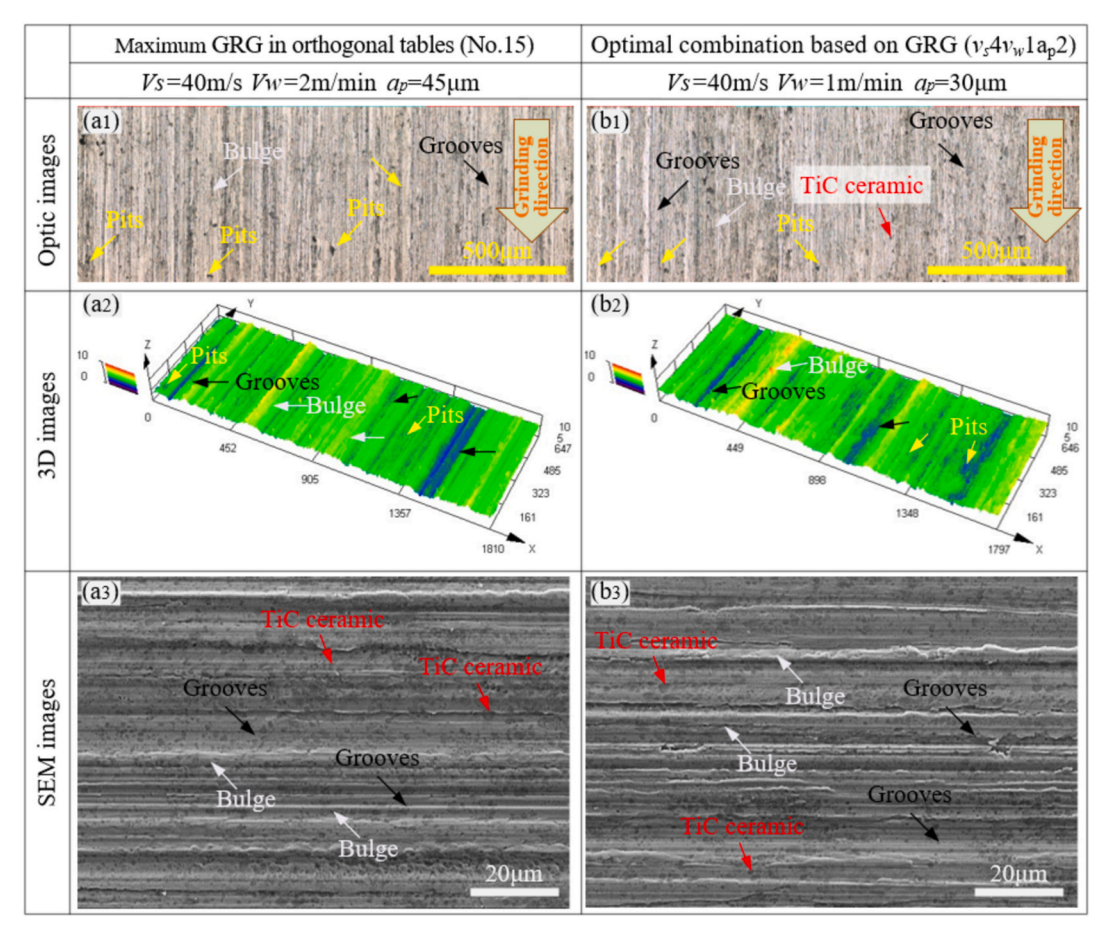


Fig. 16. Optical SEM images and 3D morphology of validation experiments.

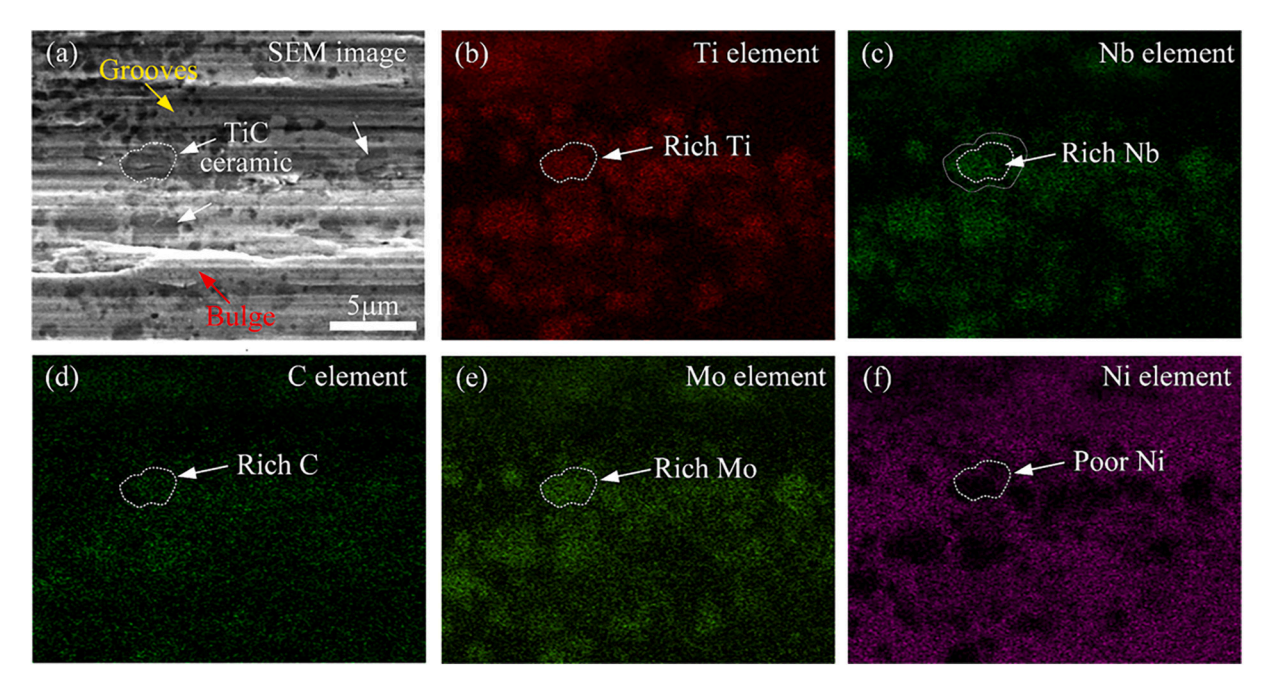


Fig. 17. SEM images and elemental distribution of ground surface for optimal combination.

process parameters are at least 7.18 %, 4.28 %, and 2.35 %, respectively.

(4) The ground surface of Laser DED ceramic reinforced Ni-based composite coatings is mainly dominated by continuous plow-

like grooves. Pits and bumps formed by brittle spalling are barely observed on the ground surface. The excellent bonding properties of the in situ synthesized ceramics to the matrix as well as the sufficiently small ceramic particles promise good grindability of the composite coatings.

# CRediT authorship contribution statement

Liaoyuan Chen: Writing – review & editing, Writing – original draft, Methodology, Investigation, Formal analysis, Data curation. Juncai Li: Validation, Software, Methodology, Data curation. Zhelun Ma: Validation, Software, Methodology. Chuang Jiang: Writing – original draft, Data curation. Tianbiao Yu: Supervision, Resources, Project administration, Funding acquisition, Conceptualization. Ruijie Gu: Writing – review & editing, Software, Funding acquisition.

# Declaration of competing interest

We declare that we have no financial and personal relationships with other people or organizations that can inappropriately influence our work, and there is no professional or other personal interest of any nature or kind in any product, service and/or company that could be construed as influencing the position presented in, or the review of, the manuscript entitled "Grinding performance and parameter optimization of laser DED TiC reinforced Ni-based composite coatings".

#### Acknowledgments

This work was financially supported by the Joint Funds of Science Research and Development Program in Henan Province (242103810048), Key Scientific Research Projects of Colleges and Universities in Henan Province (25B460003), Key Research and Development Projects in Henan Province (231111221000) and National Natural Science Foundation of China (52075088).

#### References

- [1] Bandyopadhyay A, Traxel KD, Lang M, Juhasz M, Eliaz N, Bose S. Alloy design via additive manufacturing: Advantages, challenges, applications and perspectives. Mater Today 2022;52:207–24. https://doi.org/10.1016/j.mattod.2021.11.026.
- [2] Siddiqui AA, Dubey AK. Recent trends in laser cladding and surface alloying. Optics & Laser Technology 2021;134:106619. https://doi.org/10.1016/j. optlastec.2020.106619.
- [3] Zhao Y, Yu T, Sun J, Jiang S. Microstructure and properties of laser cladded B<sub>4</sub>C/ TiC/Ni-based composite coating. Int J Refract Met Hard Mater 2020;86:105112. https://doi.org/10.1016/j.ijrmhm.2019.105112.
- [4] Chen L, Wang J, Wang Q, Zhao S, Yu T, Zhao Y. Multi-scale and multi-field coupling simulations of rapid melting and solidification process during laser DED Ni-based high-temperature alloy. Int. J Heat Mass Tran 2025;239:126538. https:// doi.org/10.1016/j.ijheatmasstransfer.2024.126538.
- [5] Zhang X, Sun Y, Yu G, Chen C, Ren X, Chen L. Microstructural evolution and high-temperature oxidation of TiC/IN625 coatings fabricated by multi-layer extreme high-speed laser cladding[J]. Optics & Laser Technology 2023;158. https://doi.org/10.1016/j.optlastec.2022.108838.
- [6] Zhu H, Ouyang M, Hu J, Zhang J, Qiu C. Design and development of TiC-reinforced 410 martensitic stainless steel coatings fabricated by laser cladding. Ceram Int 2021;47(9):12505–13. https://doi.org/10.1016/j.ceramint.2021.01.108.
- [7] Chen L, Zhao Y, Meng F, Yu T, Ma Z, Qu S, et al. Effect of TiC content on the microstructure and wear performance of in situ synthesized Ni-based composite coatings by laser direct energy deposition. Surf Coat Technol 2022;444:128678. https://doi.org/10.1016/j.surfcoat.2022.128678.
- [8] Chen L, Chen Y, Chen X, Yu T, Wang Z. Microstructure and properties of in situ TiC/Ni functionally gradient coatings by powder-fed laser cladding. Ceram Int 2022. https://doi.org/10.1016/j.ceramint.2022.08.243.
- [9] Chen L, Yu T, Guan C, Zhao Y. Microstructure and properties of metal parts remanufactured by laser cladding TiC and TiB<sub>2</sub> reinforced Fe-based coatings. Ceram Int 2022;48(10):14127–40. https://doi.org/10.1016/j. ceramint.2022.01.299.
- [10] Muvvala G, Mullick S, Nath AK. Development of process maps based on molten pool thermal history during laser cladding of Inconel 718/TiC metal matrix composite coatings. Surf Coat Technol 2020;399:126100. https://doi.org/ 10.1016/j.surfcoat.2020.126100.
- [11] Zhang M, Zhao GL, Wang XH, Liu SS, Ying WL. Microstructure evolution and properties of in-situ ceramic particles reinforced Fe-based composite coating produced by ultrasonic vibration assisted laser cladding processing. Surf Coat Technol 2020;403:126445. https://doi.org/10.1016/j.surfcoat.2020.126445.
- [12] Ni C, Zhu L, Zheng Z, Zhang J, Yang Y, Yang J, et al. Effect of material anisotropy on ultra-precision machining of Ti-6Al-4V alloy fabricated by selective laser

- melting. J Alloys Compd 2020;848:156457. https://doi.org/10.1016/j.icilloom.2020.156457
- [13] Han B, Li R, Pi Q, Shi Y, Qi H, Bi K, Sun G. Prediction of deposit characteristics based on the discrete coaxial nozzle during laser direct metal deposition. Optics & Laser Technology 2023;163:109385. 1010.1016/j.optlastec.2023.109385.
- [14] Wei HL, Liu FQ, Wei L, Liu TT, Liao WH. Multiscale and multiphysics explorations of the transient deposition processes and additive characteristics during laser 3D printing. J Mater Sci Technol 2021;77:196–208. https://doi.org/10.1016/j. imst.2020.11.032.
- [15] Qiao G, Zhang B, Bai Q, Gao Y, Du W, Zhang Y. Machinability of TiC-reinforced titanium matrix composites fabricated by additive manufacturing. J Manuf Process 2022;76:412–8. https://doi.org/10.1016/j.jmapro.2022.02.033.
- [16] Shu L, Cang X, Zhou J, Heng Z, Wu H, He W. Study on machinability and grain deformation of laser cladding manufactured and wrought IN718 alloys in dry milling process. Mater Today Commun 2023;34:105066. https://doi.org/10.1016/ i.mtcomm.2022.105066.
- [17] Xi X, Ding W, Li Z, Xu J. High speed grinding of particulate reinforced titanium matrix composites using a monolayer brazed cubic boron nitride wheel. Int J Adv Manuf Technol 2017;90(5–8):1529–38. https://doi.org/10.1007/s00170-016-9493-4.
- [18] Liu C, Ding W, Yu T, Yang C. Materials removal mechanism in high-speed grinding of particulate reinforced titanium matrix composites. Precis Eng 2018;51:68–77. https://doi.org/10.1016/j.precisioneng.2017.07.012.
- [19] Sun Y, Su Z, Jin L, Gong Y, Ba D, Yin G, et al. Modelling and analysis of microgrinding surface generation of hard brittle material machined by micro abrasive tools with helical chip pocket. J Mater Process Tech 2021;297:117242. https://doi. org/10.1016/j.jmatprotec.2021.117242.
- [20] Sun Y, Jin L, Gong Y, Wen X, Yin G, Wen Q, et al. Experimental evaluation of surface generation and force time-varying characteristics of curvilinear grooved micro end mills fabricated by EDM. J Manuf Process 2022;73:799–814. https:// doi.org/10.1016/j.jmapro.2021.11.049.
- [21] Zhang W, Wen X, Song L, Gong Y, Xu R. Experimental study on surface quality in micro-grinding FeCoNiCr high-entropy alloy prepared by selective laser melting, Arch Civ. Mech Eng 2023;24(1):27. https://doi.org/10.1007/s43452-023-00834-0.
- [22] Zhou J, Lu M, Lin J, Wei W. Influence of tool vibration and cutting speeds on removal mechanism of SiCp/Al composites during ultrasonic elliptical vibrationassisted turning. J Manuf Process 2023;99:445–55. https://doi.org/10.1016/j. imagro 2023 05 084
- [23] Qiao G, Zhang B, Guo S, Bai Q, Sun Q, Zhang Y. Surface morphology in high-speed grinding of TMCs fabricated by selective laser melting. J Manuf Process 2023;97: 200–9. https://doi.org/10.1016/j.jmapro.2023.04.064.
- [24] Zhang Z, Men X, Pan Y, Wang Z, Shi Q, Fu X. Research on simulation of SiCp/Al finite element cutting based on cohesive model. Mater Today Commun 2022;32: 103848, https://doi.org/10.1016/j.mtcomm.2022.103848.
- [25] Malakizadi A, Mallipeddi D, Dadbakhsh S, M'Saoubi R, Krajnik P. Post-processing of additively manufactured metallic alloys – A review. Int J Mach Tool Manuf 2022;179:103908. https://doi.org/10.1016/j.ijmachtools.2022.103908.
- [26] Bolar G, Das A, Joshi SN. Measurement and analysis of cutting force and product surface quality during end-milling of thin-wall components. Measurement 2018; 121:190–204. https://doi.org/10.1016/j.measurement.2018.02.015.
- [27] Ma Z, Wang Q, Chen H, Chen L, Qu S, Wang Z, et al. A grinding force predictive model and experimental validation for the laser-assisted grinding (LAG) process of zirconia ceramic. J Mater Process Tech 2022;302:117492. https://doi.org/ 10.1016/j.jmatprotec.2022.117492.
- [28] Liu Y, Liu C, Liu W, Ma Y, Tang S, Liang C, et al. Optimization of parameters in laser powder deposition AlSi10Mg alloy using Taguchi method. Optics & Laser Technology 2019;111:470–80. https://doi.org/10.1016/j.optlastec.2018.10.030.
- [29] Li M, Yu T, Yang L, Li H, Zhang R, Wang W. Parameter optimization during minimum quantity lubrication milling of TC4 alloy with graphene-dispersed vegetable-oil-based cutting fluid. J Clean Prod 2019;209:1508–22. https://doi.org/ 10.1016/j.iclepro.2018.11.147.
- [30] Wang Z, Zhang T, Yu T, Zhao J. Assessment and optimization of grinding process on AISI 1045 steel in terms of green manufacturing using orthogonal experimental design and grey relational analysis. J Clean Prod 2020;253:119896. https://doi. org/10.1016/j.jclepro.2019.119896.
- [31] Chen L, Chen Y, Chen X, Yu T, Wang Z. Microstructure and properties of in situ TiC/Ni functionally gradient coatings by powder-fed laser cladding. Ceram Int 2022;48(24):36789–801. https://doi.org/10.1016/j.ceramint.2022.08.243.
- [32] Liu S, Shin YC. The influences of melting degree of TiC reinforcements on microstructure and mechanical properties of laser direct deposited Ti6Al4V-TiC composites. Mater Design 2017;136:185–95. https://doi.org/10.1016/j.
- [33] Saroj S, Sahoo CK, Masanta M. Microstructure and mechanical performance of TiC-Inconel825 composite coating deposited on AISI 304 steel by TIG cladding process. J Mater Process Tech 2017;249:490–501. https://doi.org/10.1016/j.imatprotec.2017.06.042.
- [34] Ma Q, Li Y, Wang J. Effects of Ti addition on microstructure homogenization and wear resistance of wide-band laser clad Ni60/WC composite coatings. Int J Refract Met Hard Mater 2017;64:225–33. https://doi.org/10.1016/j.ijrmhm.2016.11.002.
- [35] Zhao Y, Chen L, Sun J, Wu W, Yu T. Microstructure evolution and wear resistance of in-situ synthesized (Ti, Nb)C ceramic reinforced Ni204 composite coatings. Ceram Int 2022. https://doi.org/10.1016/j.ceramint.2022.03.016.
- [36] Chen L, Zhao Y, Chen X, Yu T, Xu P. Repair of spline shaft by laser cladding coarse TiC reinforced Ni-based coating: Process, microstructure and properties. Ceram Int 2021. https://doi.org/10.1016/j.ceramint.2021.07.189.

- [37] Wang Q, Li Q, Zhang L, Chen DX, Jin H, Li JD, et al. Microstructure and properties of Ni-WC gradient composite coating prepared by laser cladding. Ceram Int 2022; 48(6):7905–17. https://doi.org/10.1016/j.ceramint.2021.11.338.
- [38] Xie M, Wu C, Zhou S, Jin J, Zhao S, Chen D. TiB<sub>2</sub>- and Fe<sub>2</sub>P with nanotwins-reinforced Cu-based immiscible composites fabricated by selective laser melting: Formation mechanism and wear behavior. J Alloys Compd 2021;864:158716. https://doi.org/10.1016/j.jallcom.2021.158716.
- [39] Shi Y, Li Y, Liu J, Yuan Z. Investigation on the parameter optimization and performance of laser cladding a gradient composite coating by a mixed powder of Co50 and Ni/WC on 20CrMnTi low carbon alloy steel. Optics & Laser Technology 2018;99:256–70. https://doi.org/10.1016/j.optlastec.2017.09.010.
- [40] Zhang M, Li M, Chi J, Wang S, Fang M, Zhou C, et al. In-situ (Ti,Nb)C reinforced Ni-based coatings: New insights into microstructure evolution, enhanced phase configuration behavior and tribological properties. Ceram Int 2020;46(9): 14161–72. https://doi.org/10.1016/j.ceramint.2020.02.223.
- [41] Zhao Y, Yu T, Guan C, Sun J, Tan X. Microstructure and friction coefficient of ceramic (TiC, TiN and B<sub>4</sub>C) reinforced Ni-based coating by laser cladding. Ceram Int 2019;45(16):20824–36. https://doi.org/10.1016/j.ceramint.2019.07.070.
- [42] Niu F, Bi W, Li C, Sun X, Ma G, Wu D. TiC ceramic coating reinforced 304 stainless steel components fabricated by WAAM-LC integrated hybrid manufacturing. Surf Coat Technol 2023;465:129635. https://doi.org/10.1016/j.surfcoat.2023.129635.
- [43] Beaucamp A, Simon P, Charlton P, King C, Matsubara A, Wegener K. Brittle-ductile transition in shape adaptive grinding (SAG) of SiC aspheric optics. Int J Mach Tool Manuf 2017;115:29–37. https://doi.org/10.1016/j.ijmachtools.2016.11.006.
- [44] Kishore K, Sinha MK, Chauhan SR. A comprehensive investigation of surface morphology during grinding of Inconel 625 using conventional grinding wheels. J Manuf Process 2023;97:87–99. https://doi.org/10.1016/j.jmapro.2023.04.053.
- [45] Ma Z, Wang Q, Chen H, Chen L, Meng F, Chen X, et al. Surface prediction in laser-assisted grinding process considering temperature-dependent mechanical properties of zirconia ceramic. J Manuf Process 2022;80:491–503. https://doi.org/10.1016/j.jmapro.2022.06.019.
- [46] Liang G, Zhou X, Zhao F. The grinding surface characteristics and evaluation of particle-reinforced aluminum silicon carbide. Sci Eng Compos Mater 2016;23(6): 671–6. https://doi.org/10.1515/secm-2014-0377.
- [47] Chen X, Chen L, Chen H, Song B, Zhao Y, Yu T, et al. Meso-scale numerical simulation and experimental verification of single grain grinding TiC-Fe composites. Ceram Int 2022;48(9):12299–310. https://doi.org/10.1016/j. ceramint.2022.01.091.

- [48] Wang J, Li C, Zeng M, Guo Y, Feng X, Tang L, et al. Microstructural evolution and wear behaviors of NbC-reinforced Ti-based composite coating. Int J Adv Manuf Technol 2020;107(5–6):2397–407. https://doi.org/10.1007/s00170-020-05198-
- [49] Gu P, Zhu C, Mura A, Maculotti G, Goti E. Grinding performance and theoretical analysis for a high volume fraction SiCp/Al composite. J Manuf Process 2022;76: 796–811. https://doi.org/10.1016/j.jmapro.2022.02.051.
- [50] Fathi R, Wei H, Saleh B, Radhika N, Jiang J, Ma A, et al. Past and present of functionally graded coatings: Advancements and future challenges. Appl Mater Today 2022;26:101373. https://doi.org/10.1016/j.apmt.2022.101373.
- [51] Yang Z, Zhu L, Zhang G, Ni C, Lin B. Review of ultrasonic vibration-assisted machining in advanced materials. Int J Mach Tool Manuf 2020;156:103594. https://doi.org/10.1016/j.ijmachtools.2020.103594.
- [52] Xiao G, Song K, He Y, Wang W, Zhang Y, Dai W. Prediction and experimental research of abrasive belt grinding residual stress for titanium alloy based on analytical method. Int J Adv Manuf Technol 2021;115(4):1111–25. https://doi. org/10.1007/s00170.021.07272.3
- [53] Ran Y, Kang R, Dong Z, Jin Z, Bao Y. Ultrasonic assisted grinding force model considering anisotropy of SiCf/SiC composites. Int J Mech Sci 2023;250:108311. https://doi.org/10.1016/j.ijmecsci.2023.108311.
- [54] Sun Y, Su ZP, Gong YD, Jin LY, Wen Q, Qi Y. An experimental and numerical study of micro-grinding force and performance of sapphire using novel structured micro abrasive tool. Int J Mech Sci 2020;181:105741. https://doi.org/10.1016/j. iimecsci 2020 105741
- [55] Li M, Yu T, Yang L, Li H, Zhang R, Wang W. Parameter optimization during minimum quantity lubrication milling of TC4 alloy with graphene-dispersed vegetable-oil-based cutting fluid. J Clean Prod 2019;209:1508–22. https://doi.org/ 10.1016/j.jclepro.2018.11.147.
- [56] Yang Z, Zhu L, Ni C, Ning J. Investigation of surface topography formation mechanism based on abrasive-workpiece contact rate model in tangential ultrasonic vibration-assisted CBN grinding of ZrO<sub>2</sub> ceramics. Int J Mech Sci 2019; 155:66–82. https://doi.org/10.1016/j.ijmecsci.2019.02.031.
- [57] Sun S, Fu H, Ping X, Lin J, Lei Y, Wu W, et al. Reinforcing behavior and microstructure evolution of NbC in laser cladded Ni45 coating. Appl Surf Sci 2018; 455:160–70. https://doi.org/10.1016/j.apsusc.2018.05.199.
- [58] Xi W, Song B, Sun Z, Yu T, Wang J, Sun Q. Effect of various morphology of in situ generated NbC particles on the wear resistance of Fe-based cladding. Ceram Int 2023;49(7):10265–72. https://doi.org/10.1016/j.ceramint.2022.11.206.